

# Water Resources Research®

## RESEARCH ARTICLE

10.1029/2022WR032227

### Key Points:

- We developed a framework to construct the clear-sky diurnal cycle of ECOSTRESS land surface temperature (LST) and evapotranspiration (ET)
- The diurnally resolved 70 m LST/ET successfully reproduced the fine spatial variation in the native ECOSTRESS measurements
- The diurnally resolved LST/ET well captured the diurnal variation of independent in situ measurements, especially on clear-sky conditions

### Supporting Information:

Supporting Information may be found in the online version of this article.

### Correspondence to:

J. Wen and Y. Sun,  
jw2495@cornell.edu;  
ys776@cornell.edu

### Citation:

Wen, J., Fisher, J. B., Parazoo, N. C., Hu, L., Litvak, M. E., & Sun, Y. (2022). Resolve the clear-sky continuous diurnal cycle of high-resolution ECOSTRESS evapotranspiration and land surface temperature. *Water Resources Research*, 58, e2022WR032227. <https://doi.org/10.1029/2022WR032227>

Received 18 FEB 2022  
Accepted 25 AUG 2022

### Author Contributions:

**Conceptualization:** Jiaming Wen, Ying Sun

**Data curation:** Jiaming Wen, Joshua B. Fisher

**Formal analysis:** Jiaming Wen, Joshua B. Fisher, Leiqui Hu, Ying Sun

**Funding acquisition:** Nicholas C. Parazoo, Ying Sun

**Methodology:** Jiaming Wen, Joshua B. Fisher, Leiqui Hu, Ying Sun

**Project Administration:** Nicholas C. Parazoo, Ying Sun

**Supervision:** Ying Sun

**Validation:** Marcy E. Litvak

**Writing – original draft:** Jiaming Wen, Ying Sun

© 2022. American Geophysical Union.  
All Rights Reserved.

## Resolve the Clear-Sky Continuous Diurnal Cycle of High-Resolution ECOSTRESS Evapotranspiration and Land Surface Temperature

Jiaming Wen<sup>1</sup> , Joshua B. Fisher<sup>2</sup> , Nicholas C. Parazoo<sup>3</sup> , Leiqui Hu<sup>4</sup> , Marcy E. Litvak<sup>5</sup> , and Ying Sun<sup>1</sup> 

<sup>1</sup>School of Integrative Plant Science, Soil and Crop Sciences Section, Cornell University, Ithaca, NY, USA, <sup>2</sup>Schmid College of Science and Technology, Chapman University, Orange, CA, USA, <sup>3</sup>Jet Propulsion Laboratory, California Institute of Technology, Pasadena, CA, USA, <sup>4</sup>Department of Atmospheric and Earth Science, University of Alabama in Huntsville, Huntsville, AL, USA, <sup>5</sup>Department of Biology, University of New Mexico, Albuquerque, NM, USA

**Abstract** Although numerous evapotranspiration (ET) estimates have been developed from remote sensing measurements, a diurnally resolved product with high spatial resolution (<100 m) is still lacking, which is critically needed for agricultural and ecological monitoring. The ECOSystem Spaceborne Thermal Radiometer Experiment on Space Station (ECOSTRESS) provides, for the first time, ET at 70 m resolution with diurnal samplings, enabling a step toward filling this data gap. This study developed the first framework to resolve the full diurnal cycle of ET and Land Surface Temperature (LST) from sporadic ECOSTRESS measurements. We first constructed 70 m diurnal LST utilizing a diurnal temperature cycle (DTC) model that fused ECOSTRESS and Geostationary Operational Environmental Satellite (GOES) LST. Next, we derived 70 m diurnal ET from the diurnally resolved LST, along with ancillary meteorological and reflectance data sets, using the Priestley-Taylor Jet Propulsion Laboratory (PT-JPL) algorithm. This framework was tested in two regions: A relatively homogeneous semiarid grassland landscape (centered at the US-Seg Ameriflux site) and a heterogeneous humid cropland landscape (centered at US-ARM). Our diurnally resolved LST and ET successfully reproduced the spatial patterns in the native ECOSTRESS measurements during overpasses for both landscapes (LST:  $r > 0.97$ , RMSE  $\sim 2^\circ\text{C}$ ; ET:  $r > 0.99$ , and RMSE = 1–7 W m $^{-2}$ ). The constructed time series also well captured the temporal variability of the in situ measurements (especially under clear-sky conditions) at both US-Seg and US-ARM, albeit performance varying with availability and quality of ECOSTRESS samples. This study sets the stage for testing and applying our framework to broader climates, biomes, and landscapes toward eventually generating diurnally resolved 70 m global operational LST/ET products to enhance ecological/agricultural applications.

## 1. Introduction

Terrestrial evapotranspiration (ET), consisting of plant canopy transpiration and evaporation from soil and canopy interception, is a key hydrological variable that strongly interacts with the terrestrial carbon cycle, regulates land-atmosphere energy exchanges, and feeds back to the climate system (Bonan, 2008; Fisher et al., 2017; Wang & Dickinson, 2012). Accurate estimation of ET is critical for quantifying the water and energy balance of the Earth system and providing key information for water resource and agriculture management (Allen et al., 1998, 2005; Anderson et al., 2012; Sahoo et al., 2011).

A number of approaches and platforms have been employed to measure/estimate ET across different temporal and spatial scales. Ground-based measurements, for example, from lysimeters (Goss & Ehlers, 2009), energy balance Bowen ratio systems (Bowen, 1926; Cook, 2007), or eddy covariance (EC) towers (Baldocchi, 2014; Baldocchi et al., 1988), are well-established for continuously measuring terrestrial ET at high frequency, for example, over diurnal courses. However, such measurements have limited spatial coverage (e.g., ~1 km footprint size for EC towers) and are sparsely and unevenly distributed across the globe, with even fewer in remote tropical and boreal regions (Falge et al., 2017; Schimel & Schneider, 2019). At large scale, ET at basin or continental scales has been estimated based on the water budget balance (Ramillien et al., 2006), but it is challenging to resolve ET contribution at finer spatial scales. In the past decades, advances in satellite remote sensing have enabled numerical methods to estimate global gridded ET with remotely sensed variables as inputs, such as solar radiation, air temperature, humidity, surface albedo, leaf area index, etc. These methods can be broadly classified into

**Writing – review & editing:** Jiaming Wen, Joshua B. Fisher, Nicholas C. Parazoo, Leiqui Hu, Marcy E. Litvak, Ying Sun

two categories: (a) Physics-based models based on the Penman–Monteith (PM) equation (Jiang & Ryu, 2016; Monteith, 1965; Mu et al., 2007, 2011; Running et al., 2017; Senay, 2018; Senay et al., 2007, 2011; Su, 2002; Yuan et al., 2010), or the Priestley–Taylor (PT) equation (Anderson et al., 1997, 2011; Fisher et al., 2008; Miralles et al., 2011; Priestley & Taylor, 1972), or recently the complementary theory (Bouchet, 1963; Brutsaert, 2015; Brutsaert et al. 2020; Ma et al., 2019), with various assumptions and formulations (e.g., some are coupled with surface energy balance (SEB) equations and photosynthesis models) and (b) statistical or machine learning-based models (Bedesheim et al., 2018; Jung et al., 2009, 2011, 2019; Tramontana et al., 2016; Yang et al., 2006).

However, these remote sensing-based ET data sets are limited by their coarse spatial and/or temporal resolutions. For example, Moderate Resolution Imaging Spectroradiometer (MODIS) ET (Running et al., 2017) and Breathing Earth System Simulator (BESS) ET (Jiang & Ryu, 2016) are offered at 1 km and an 8-day resolution. Products with daily or subdaily resolution, however, have coarse spatial resolution, for example, Geostationary Operational Environmental Satellite (GOES) ET at a spatial resolution of 2 km (Fang et al., 2019), Global Land surface Evaporation: the Amsterdam Methodology (GLEAM) ET at 0.25° (Miralles et al., 2011), and the upscaled FLUXNET ET at 0.5° (Bedesheim et al., 2018). ET, in reality, varies substantially in space (e.g., subfield) and is highly dynamic in time (e.g., subdaily), in response to highly dynamic weather variations (i.e., radiation, air temperature, humidity, and wind speed), and affected by land cover, soil properties, soil moisture, topography, and vegetation types. Without concurrently resolving the high spatial and temporal variations, the full potential of remote sensing ET products for operational applications (e.g., agriculture monitoring, water resource management, and ecological forecasting) is limited (Fisher et al., 2017). Several emerging studies have started to address this issue. For example, Anderson et al. (2021) developed a framework to provide ET data at 30 m daily resolution by fusing retrievals from GOES, MODIS, Landsat, and the recently launched ECOSystem Spaceborne Thermal Radiometer Experiment on Space Station (ECOSTRESS). In their studies, instantaneous ET from different satellites was scaled to daily integral assuming a constant ratio between ET and incoming solar radiation (e.g., Cammalleri et al., 2014). Although such assumption may capture the first-order diurnal variations in ET, solar radiation alone is insufficient to characterize the full diurnal dynamics in ET influenced by other abiotic and biotic factors described above (Cammalleri et al., 2014; Dhungel et al., 2021; Nelson et al., 2018; Renner et al., 2019; Zhang et al., 2014; Zheng et al., 2014). Therefore, a more realistic diurnal ET product should consider all these factors in order to minimize potential biases (e.g., stomatal closure due to water stress at the subdaily scale), which contributes to more accurate ET estimation at longer time scales, for example, seasonal, annual, and beyond.

ECOSTRESS, launched in June 2018, holds great potential to provide ET products at both high spatial (<100 m) and temporal (subdaily) resolutions. It measures thermal infrared radiation (TIR) in five bands from 8 to 12.5 μm at a nominal footprint size of 38 m × 69 m every 1–5 days with diurnal sporadic sampling (i.e., passing over the same spot at different times of day for each revisit) (Fisher et al., 2020). Based on the measured radiance, different levels of products are generated. For example, a land surface temperature (LST) product is generated using the Temperature and Emissivity Separation retrieval algorithm (Gillespie et al., 1998; Hulley et al., 2021; Hulley & Hook, 2011). ET, the major scientific focus of ECOSTRESS, is estimated based on this LST retrieval along with ancillary vegetation and meteorological data sets (mostly from MODIS and Landsat) using the Priestley–Taylor Jet Propulsion Laboratory (PT-JPL) algorithm (Fisher et al., 2008, 2020) or Atmosphere Land Exchange Inverse Disaggregation algorithm (DisALEXI, Anderson et al., 2011; Cawse-Nicholson et al., 2020). Here, LST retrieved from thermal remote sensing is critical in accurately calculating energy balance and determining soil moisture status for land surface with different land cover types (Fisher et al., 2017), and hence one of the major input variables for estimating ECOSTRESS ET. Higher level products such as Evaporative Stress Index (ESI) and water use efficiency (WUE), which are dependent on ET estimates, are also provided. The high spatial resolution and 1–5 days revisit cycle of ECOSTRESS enables new opportunities such as timely crop monitoring at field and subfield scales. The diurnal sampling characteristics of ECOSTRESS can provide key insight about diurnal variations (Xiao et al., 2021). For example, the afternoon overpasses may reflect heat stress that can result in stomatal closure and decreased ET, which may not be captured by satellites with only morning overpass time. However, this sampling strategy also imposes great challenges on directly inferring changes from two different overpasses without resolving the full diurnal cycle.

In this paper, we aim to remedy this issue by developing a framework to construct the full diurnal cycle of ECOSTRESS ET and LST from sporadic native ECOSTRESS measurements at high spatial resolution (70 m) under clear-sky conditions. As the first study of its kind, we demonstrated the effectiveness and scalability of our frame-

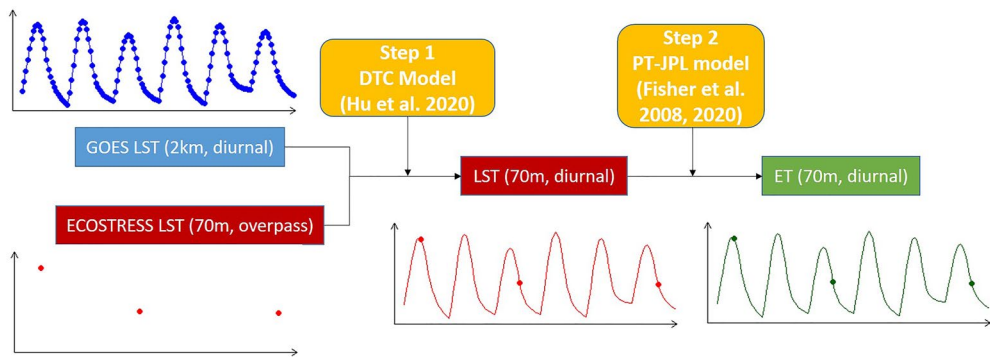


**Figure 1.** The overall framework for constructing the full diurnal cycle of land surface temperature (LST) and evapotranspiration (ET) from sporadic ECOSTRESS measurements.

work in a relatively homogeneous semiarid grassland landscape and a heterogeneous humid cropland landscape. This framework is generic and has the potential to be expanded to broader climates and biome types, setting the stage for eventually applying it for generating operational clear-sky global 70 m diurnally resolved LST and ET products. This will substantially enhance the real time monitoring capability of Earth surface at concurrently fine spatial and temporal resolutions that are previously impossible.

## 2. Methodology

### 2.1. The Overall Framework

To generate diurnally resolved and high spatial resolution LST and ET products from the native ECOSTRESS sporadic measurements, our framework consists of two steps (illustrated in Figure 1). First, we constructed the diurnal cycle of ECOSTRESS LST using a diurnal temperature cycle (DTC) model initially developed by Götsche and Olesen (2001) and widely adopted and refined afterward (Duan et al., 2014; Hu et al., 2020). Second, we utilized the PT-JPL algorithm (Fisher et al., 2008, 2020), which has been employed by the ECOSTRESS team for deriving its operational ET (PT-JPL) product, to construct diurnally resolved ECOSTRESS LST. Detailed procedures are provided below.

### 2.2. The DTC Model

The DTC model employed in this study was originally developed by Götsche and Olesen (2001). It assumes that the clear-sky LST can be represented as a harmonic function during daytime and a hyperbolic decay after sunset (Figure 2) based on the physical processes of thermal diffusion and Newton's Law of cooling. This model was further modified by Duan et al. (2014) and Hu et al. (2020, Equation 1) to construct the full diurnal cycle of MODIS LST.

$$\text{LST}(t) = T_0 + T_a \cos\left(\frac{\pi}{\omega}(t - t_{\max})\right) \quad t < t_s \quad (1a)$$

$$\text{LST}(t) = (T_0 + \delta T) + \left[ T_a \cos\left(\frac{\pi}{\omega}(t_s - t_{\max})\right) - \delta T \right] \frac{k}{k + t - t_s} \quad t \geq t_s \quad (1b)$$

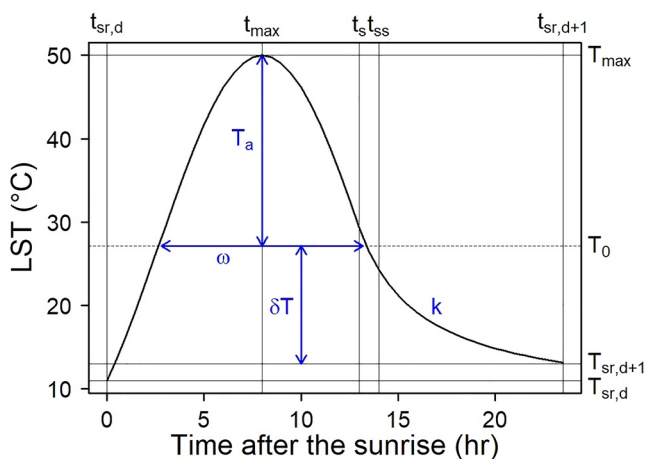


**Figure 2.** A schematic illustration of the diurnal temperature cycle (DTC) model. Definition of notations and their calculations can be found in Appendix A.

where  $\text{LST}(t)$  denotes LST at time  $t$ . Here, the unknown parameters in the DTC model that need to be determined with observations include LST at sunrise of day  $d$  and  $d + 1$  ( $T_{\text{sr},d}$ ,  $T_{\text{sr},d+1}$ ), LST maximum of day  $d$  ( $T_{\max,d}$ ), time when LST reaches its daily maximum ( $t_{\max}$ ), and time of thermal sunset when the nighttime attenuation starts ( $t_s$ ). These parameters can be categorized into two groups: Time-related ( $t_{\max}$ ,  $t_s$ ) and temperature-related ( $T_{\text{sr},d}$ ,  $T_{\text{sr},d+1}$ ;  $T_{\max,d}$ ), which were fitted pixel by pixel. To construct the full diurnal cycle from sporadic measurements of ECOSTRESS LST, we adopted a similar strategy of Hu et al. (2020), detailed below.

First, we fit the time-related parameters ( $t_{\max}$ ,  $t_s$ ) with the high-frequency LST measurements from GOES (although at relatively lower spatial resolution) during each 10-day window, assuming these parameters are not sensitive to systematic differences among different LST products. The time-related parameters are assumed to be constant across all fine ECOSTRESS pixels within each single coarse GOES pixel.

Once the time-related parameters were determined, we then fit the temperature-related parameters ( $T_{sr,d}$ ,  $T_{sr,d+1}$ ,  $T_{\max,d}$ ) with sporadic LST measurements from ECOSTRESS. The temperature-related parameters of all the days during each selected period (i.e., a 10-day time window) were fitted altogether. For example, for a 10-day time window, we fit 21 temperature-related parameters ( $T_{sr,d}$  from Day 1 to Day 11,  $T_{\max,d}$  from Day 1 to Day 10) in total. As there were typically only about four ECOSTRESS observations available during a 10-day window, it would be an underdetermined problem to fit solely with ECOSTRESS observations. Therefore, to mitigate this issue, we employed two strategies to take advantage of GOES LST observations that are much more frequently available.

The first strategy was to assume that the day-to-day difference in the fitted  $T_{\max,d}$  (and  $T_{sr,d}$ ) (between any 2 days) for the fine ECOSTRESS pixel remains the same as that for the corresponding coarse GOES pixel. With this assumption, the number of temperature-related parameters that need to be fit (constrained) with ECOSTRESS LST can be effectively reduced, from 21 to 2, that is, only  $T_{sr,d}$  and  $T_{\max,d}$  on a single day. Note that ECOSTRESS LST on other days could still contribute to the fitting through the enforced day-to-day variation constraint.

The second strategy was that when fitting  $T_{sr,d}$  and  $T_{\max,d}$  on a single day with ECOSTRESS LST, we also included GOES LST as an additional constraint. This constraint can take advantage of hourly GOES observations and therefore improve the robustness of fitting. Specifically, we set the loss function to be as follows:

$$f_{\text{loss}} = \text{nRMSE} \left( \text{LST}_{\text{ECOSTRESS}}, \hat{\text{LST}}_{\text{ECOSTRESS}} \right) + \theta \cdot \text{nRMSE} \left( \text{LST}_{\text{GOES}}, \hat{\text{LST}}_{\text{GOES}} \right) \quad (2)$$

$$\text{nRMSE}(y, \hat{y}) = \sqrt{\sum_{i=1}^n \left( \frac{y_i - \hat{y}_i}{\hat{y}_i} \right)^2 / n} \quad (3)$$

where nRMSE stands for normalized RMSE,  $y$  is observation,  $\hat{y}$  is prediction,  $n$  is the number of observations of ECOSTRESS or GOES observations in each fitting window,  $i$  is the index of each observation,  $\theta$  is a weighting factor determined with leave-one-out cross validation (details in Section 2.4). Here, a larger  $\theta$  means adding GOES LST can contribute to higher fitting accuracy, resulting from greater LST consistency between the coarse GOES pixel and the fine ECOSTRESS pixel; a smaller  $\theta$ , in contrast, means LST from the coarse GOES pixel has larger discrepancy from that of the fine ECOSTRESS pixel, in which case, the fitting would rely less on GOES LST. This parameter  $\theta$  can effectively account for the discrepancies between coarse GOES pixels and fine ECOSTRESS pixels due to differences in instruments or retrieval algorithms, especially subgrid heterogeneity within GOES pixels.

With these two constraints, the model fit can be better constrained on days when ECOSTRESS observations are not available.

### 2.3. The PT-JPL ET Model

The PT-JPL model (Fisher et al., 2008) first starts with the Priestley and Taylor (1972) equation that estimates potential evapotranspiration (PET) from net radiation ( $R_n$ ) and air temperature ( $T_{\text{air}}$ ). LST, which determines the upwelling longwave radiation ( $LW_{\text{out}}$ ), is a major contributor to the spatial variability of  $R_n$  and therefore is a key input to compute PET. The PT-JPL model then scales PET to estimate the three components of actual ET separately (Equations 4–7, Figure 3), that is, plant canopy transpiration ( $ET_c$ ), evaporation from soil ( $ET_s$ ), and evaporation from canopy interception ( $ET_i$ ), down-regulated by a number of constraints from temperature, moisture content, and vegetation fraction. Note that all the ET terms are in the unit of  $\text{W m}^{-2}$  here, denoting the latent heat required to convert liquid water in soils and plants into vapor.

$$ET = ET_c + ET_s + ET_i \quad (4)$$

$$ET_c = (1 - f_{\text{wet}}) f_g f_T f_M \alpha \frac{\Delta}{\Delta + \gamma} R_{\text{nc}} \quad (5)$$

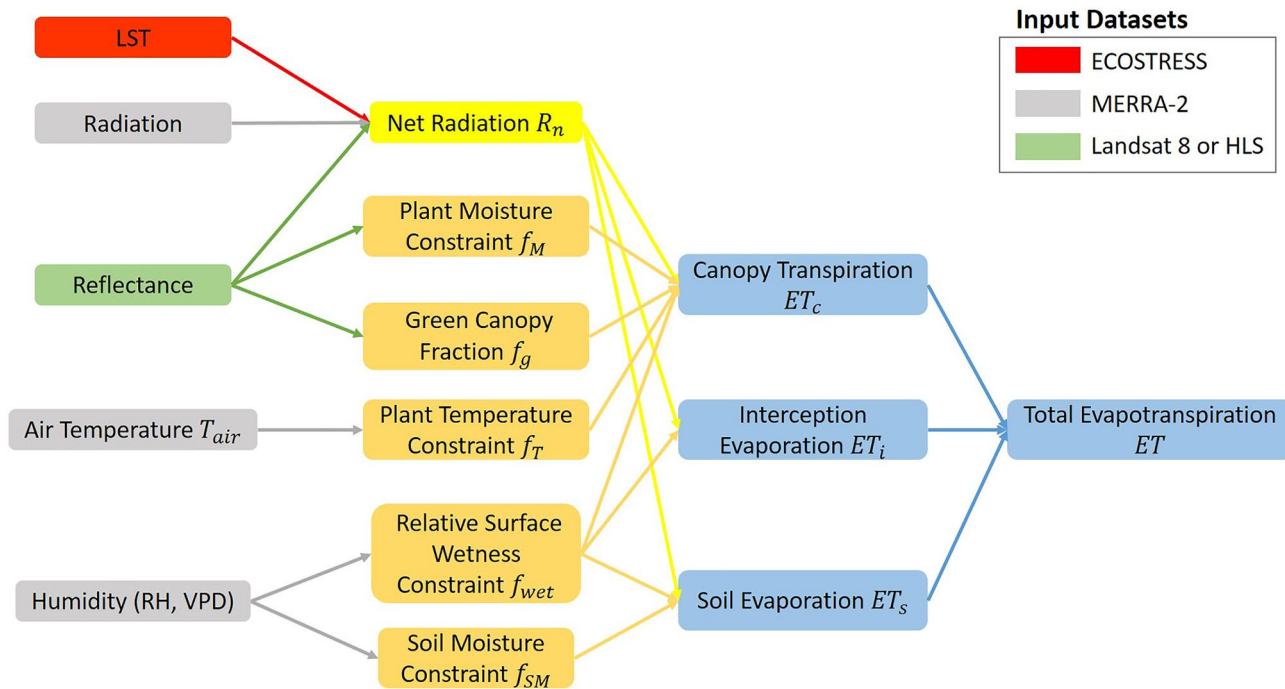


**Figure 3.** Diagram of the PT-JPL model. Land surface temperature (LST) from ECOSTRESS (red) along with meteorological data sets from MERRA-2 reanalysis (gray, Table B5) and surface reflectance from Landsat 8 or Harmonized Landsat and Sentinel-2 (HLS) (green, Table B4) are used to calculate net radiation (yellow, Table B3) and constraint factors (orange, Table B2), which are ultimately used to estimate evapotranspiration (ET) components and total ET (blue, Table B1).

$$ET_s = (f_{wet} + f_{SM}(1 - f_{wet})) \alpha \frac{\Delta}{\Delta + \gamma} (R_{ns} - G) \quad (6)$$

$$ET_i = f_{wet} \alpha \frac{\Delta}{\Delta + \gamma} R_{nc} \quad (7)$$

where  $R_{nc}$ ,  $R_{ns}$ , and  $G$  denote net radiation for canopy and soil, and ground heat flux, respectively. Other notations and calculations are provided in Appendix B.

This algorithm was originally used to estimate monthly ET at  $1^{\circ}$  grids globally (Fisher et al., 2008) and is effective in characterizing the seasonal variation of flux tower ET (Chen et al., 2014; Ershadi et al., 2014; Fisher et al., 2008; Gomis-Cebolla et al., 2019; McCabe et al., 2016; Michel et al., 2016; Miralles et al., 2016; Vinukollu et al., 2011). To estimate instantaneous ET at high spatial resolution (70 m) and at different times of day during the overpass of ECOSTRESS, two major changes were made by the ECOSTRESS team: (a) Finer spatial resolution data sets from MODIS and Landsat were employed and (b) meteorological variables (e.g.,  $R_n$ ,  $T_a$ , and  $e_a$ ) were diurnally interpolated to the overpass time. For detailed information, please refer to Fisher and ECOSTRESS algorithm development team. (2015); Halverson (2018); Fisher et al. (2020). ECOSTRESS ET showed overall consistent agreement with flux tower ET when measurements from all selected sites and time periods were pooled together (Fisher et al., 2020), indicating the overall effectiveness of PT-JPL in estimating subdaily ET. The ancillary data sets used in this study are described in Section 3.2.3.

#### 2.4. Performance Evaluation

We employed two approaches to assess the performance of the diurnally resolved ECOSTRESS LST and ET. First, we utilized leave-one-out cross validation to check the consistency with the native ECOSTRESS observations. Leave-one-out cross validation is a widely used approach for evaluating out-of-sample performance, especially for scenarios under which data samples are not sufficient (Hastie et al., 2009). In our case, ECOSTRESS data acquisition is relatively sparse in time, we therefore withheld each overpass and used the remaining overpasses for model fitting; the fitted models were then used for prediction at the withheld overpass time, which in turn was

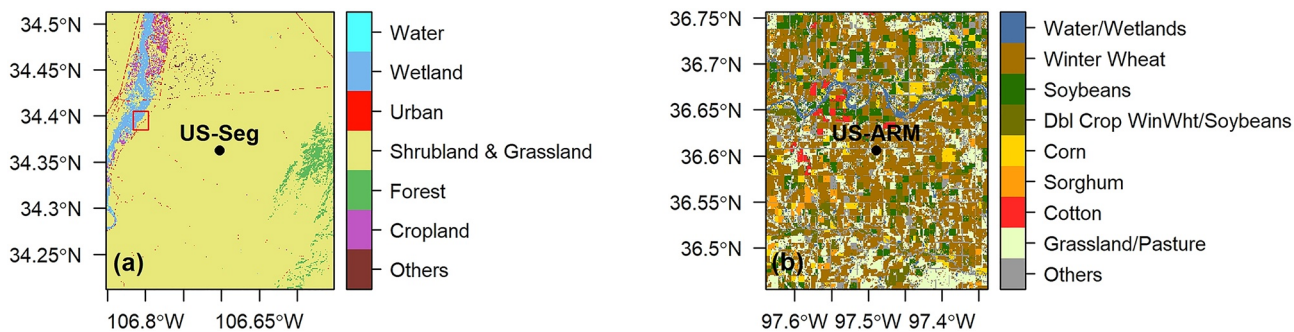


**Figure 4.** The land cover map of our study domains. The flux towers (US-Seg and US-ARM) are located in the center, marked with black dots. The red square in (a) represents the location of the tested GOES pixel in Section 5.1 and Figure 17. The land cover type data set is from USDA National Agricultural Statistics Service Cropland Data Layer (2020, <https://nassgeodata.gmu.edu/CropScape>).

compared with the native ECOSTRESS measurements. This leave-one-overpass-out approach can best mimic the real scenario of filling the diurnal gaps when continuous ECOSTRESS observations are not available.

Second, we evaluated the temporal variations of the diurnally resolved ECOSTRESS LST and ET with independent flux tower measurements (details in Section 3.1). In this case, all available ECOSTRESS overpasses were used for model fitting.

We utilized a suite of metrics to evaluate the model performance, including Pearson correlation coefficient ( $r$ ), Nash-Sutcliffe modeling efficiency (MEF; Nash & Sutcliffe, 1970), root-mean-square error (RMSE), and mean Bias.  $r$ , ranging from  $-1$  to  $1$ , measures the linear correlation between prediction and observation. MEF, ranging from  $-\infty$  to  $1$ , evaluates the performance of the model compared to predicting as observation mean (in such case,  $MEF = 0$ ). RMSE measures the average magnitude of the prediction residuals. Bias measures the difference between observation mean and prediction mean. Higher  $r$  and MEF (closer to  $1$ ) and lower RMSE and bias (closer to  $0$ ) mean greater consistency between model predictions with observations.

$$r = \frac{\sigma_{y\hat{y}}}{\sigma_y \sigma_{\hat{y}}} \quad (8)$$

$$MEF = 1 - \frac{\sum_{i=1}^n (\hat{y}_i - y_i)^2}{\sum_{i=1}^n (\hat{y}_i - \bar{y})^2} \quad (9)$$

$$RMSE = \sqrt{\frac{\sum_{i=1}^n (\hat{y}_i - y_i)^2}{n}} \quad (10)$$

$$Bias = \frac{\sum_{i=1}^n (\hat{y}_i - y_i)}{n} \quad (11)$$

where  $y$  is observation,  $\hat{y}$  is prediction,  $n$  is the number of observations, and  $i$  is the index of each observation;  $\bar{y}$  is the mean of observations;  $\sigma_y$  and  $\sigma_{\hat{y}}$  are the standard deviations of observations and predictions, respectively; and  $\sigma_{y\hat{y}}$  is the covariance between observations and predictions.

### 3. Study Domain and Data Sets

#### 3.1. Study Domains and Time Periods

The performance of our developed framework was tested at two  $0.3^\circ \times 0.3^\circ$  (approximately  $30 \text{ km} \times 30 \text{ km}$ ) domains with distinct vegetation types, landscape heterogeneities, and climate regimes (Figure 4). The first test domain is centered at a semiarid grassland EC flux tower US-Seg ( $106.7020^\circ\text{W}$ ,  $34.3623^\circ\text{N}$ , Anderson-Teixeira et al., 2011; Duman et al., 2021) located at the Sevilleta Wildlife Refuge. This is a core site of Ameriflux since 2013 and within the Long Term Ecological Research (LTER) program. The mean annual temperature at this site is  $13.7^\circ\text{C}$  and mean annual precipitation is 273 mm. The dominant land cover type in this study domain is desert

**Table 1**

Comparison of Characteristics for LST Data Sets Used in This Study

	Spatial resolution	Temporal resolution	Platform characteristics
GOES	2 km	Hourly	Geostationary orbit, discrete data acquisition throughout the day
ECOSTRESS	70 m	1–5 days	Low Earth orbit, sporadic overpass with diurnal sampling
In situ	several meters	half-hourly	In situ measurement, continuous data acquisition throughout the day

shrublands and C4 grasslands, with some mid elevation woodlands (forests) located in the southeast and riparian vegetation (wetlands) and croplands near the Rio Grande river in the northwest (Figure 4a). We chose this domain mainly for two reasons: (a) Located in a dry region, it is less affected by clouds and offers good availability of remote sensing measurements and (b) despite the dominance of semiarid vegetation, the presence of other vegetation types (e.g., croplands, wetlands, and forests) provides an opportunity for also testing our framework with a diverse range of land covers. In this domain, we used three 10-day time windows at distinct phenological stages to test the robustness of our framework: (a) Peak growing season, 4–14 August 2018; (b) green-up stage, 7–17 April 2020; and (c) senescence stage, 26 September–5 October 2020. These three time windows were selected mainly because of their availability of good quality data from ECOSTRESS (Section 3.2.1). The third window was primarily sunny, while the first two windows experienced a strong storm during 10–11 August 2018 and a rain event on 13 April 2020, respectively (Figure S1 in Supporting Information S1), with some local temporary clouds on other days (e.g., 6 August 2018 and 12 April 2020). We hypothesized that the performance of the framework can be influenced by the occurrence of rain events and clouds during the first two windows, when fewer satellite observations (ECOSTRESS, GOES, and ancillary data sets) with acceptable quality were available for model fitting.

The second test domain is centered at a humid cropland EC flux tower US-ARM (97.4888°W, 36.6058°N, Fischer et al., 2007) in Lamont, Oklahoma. The mean annual temperature at this site is 14.76°C and mean annual precipitation is 843 mm. This study domain is mostly covered by various crop types, dominated by winter wheat and soybean (Figure 4b). We chose this domain to further test the effectiveness of our framework in heterogeneous landscapes. We selected one time window, that is, 15–19 June 2021, during the harvesting stage for winter wheat and planting stage for soybean.

The half-hourly meteorological and flux data at US-Seg and US-ARM were obtained from Ameriflux (<https://ameriflux.lbl.gov>) with standard quality assessment (Biraud et al., 2021; Litvak, 2021). The in situ LST and ET time series at these two sites were used for evaluating our diurnally resolved ECOSTRESS LST and ET. As there were no direct measurements of LST from the tower, we estimated LST with upward longwave radiation and surface emissivity (Equation 12, Hu et al., 2020).

$$\text{LST} = \left[ \frac{\text{LW}_{\text{out}} - \text{LW}_{\text{in}}(1 - \varepsilon)}{\sigma \cdot \varepsilon} \right]^{\frac{1}{4}} \quad (12)$$

where  $\text{LW}_{\text{out}}$  is upward longwave radiation and  $\text{LW}_{\text{in}}$  is downward longwave radiation, measured at each tower;  $\varepsilon$  is surface emissivity, from ECOSTRESS overpasses at tower location averaged for each time window; and  $\sigma$  is the Stefan-Boltzmann constant ( $5.67 \times 10^{-8} \text{ W m}^{-2} \text{ K}^{-4}$ ). Although the footprint size is only several meters for the tower LST (Table 1) and hundreds of meters for ET, we extracted the constructed LST and ET averaged from  $5 \times 5$  adjacent ECOSTRESS pixels (350 m × 350 m) centered at each tower for comparison. Within this range, ECOSTRESS LST and ET showed little variation, therefore well representing the hydroclimatic and landscape characteristics of the towers.

Note that the in situ LST and ET measurements at EC towers can have large uncertainties on rainy days, which prevent their validity to be used for evaluating our framework. Therefore, we excluded the rainy days (10–11 August 2018 and 13 April 2020) from model evaluation at US-Seg. For nonrainy days, we further evaluated the constructed LST against the in situ LST separately for clear-sky (cloud fraction,  $\text{CF} \leq 0.2$ , Figure S1 in Supporting Information S1) and cloudy conditions ( $\text{CF} > 0.2$ ) at US-Seg to investigate the degree to which cloudy conditions can influence the fitting of DTC. Here CF is defined as follows:

$$\text{CF}_i = 1 - (\text{SW}_{\text{in}})_i / \max(\text{SW}_{\text{in}})_i \quad (13)$$

**Table 2**

Data Input for the PT-JPL Model Used in the Operational ECOSTRESS ET Product and This Study

Variables	Operational ECOSTRESS ET product	This study
LST and $\epsilon$	ECOSTRESS	ECOSTRESS
Reflectances	Landsat 8, MODIS, Visible Infrared Imaging Radiometer Suite (VIIRS)	Landsat 8, HLS
$SW_{in}$ , $SW_{out}$ , $LW_{in}$	Forest Light Environmental Simulator (FLIES) with MODIS <sup>a</sup>	MERRA-2, Landsat 8, HLS
$T_{air}$ , $T_{dew}$	MODIS <sup>a</sup>	MERRA-2

<sup>a</sup>Changed to GEOS-FP products in Collection 2.

where  $SW_{in}$  is the incoming shortwave radiation,  $i$  is the index for time of day, and  $\max(SW_{in})$  is the maximum of  $SW_{in}$  at the same time of day for each 10-day windows, which can be considered as the potential  $SW_{in}$  under clear-sky conditions.

### 3.2. Data Sets

#### 3.2.1. ECOSTRESS

We obtained ECOSTRESS LST and ET data (software build id 0601) along with their quality layers gridded at 70 m from the Application for Extracting and Exploring Analysis Ready Samples (AppEEARS) tool (AppEEARS Team, 2020). All the ECOSTRESS images used in this study were acquired and processed for daytime only. For data quality control, we selected pixels flagged with (a) “Pixel produced, best quality” and “Pixel produced, nominal quality” in the quality layer; (b) “Cloud Mask Flag determined,” “no Final Cloud Plus Region-growing,” and “no Final Cloud, either one of bits 2, 3, or 4 set” in the cloud mask layer. We discarded images with more than 50% pixels of poor quality. After this data filtering, there were four, four, and six remaining overpasses for LST, and four, four, and five for ET during the three selected time windows, respectively, for the test domain centered at US-Seg. For the domain centered at US-ARM, there were four overpasses for LST and three for ET during the selected time window. ET data is sometimes less than LST because the availability of ET also depends on the availability of other ancillary data required by the PT-JPL model (Sections 2.3, 3.2.3) besides LST.

#### 3.2.2. GOES LST

We obtained geostationary LST from GOES-16 (Menzel & Purdom, 1994; Yu et al., 2009), which was launched in December 2017 and provides hourly LST data at a resolution of 2 km over the continental United States (CONUS). Only observations flagged with good retrieval quality were used in this study. To check the consistency between ECOSTRESS and GOES LST, we made a direct comparison between them for the two tested domains and four selected time windows. To match the spatial and temporal resolutions of ECOSTRESS, here GOES LST was interpolated spatially (using bilinear interpolation) and temporally (using 2nd order polynomial interpolation with three nearby hourly observations). Our results confirmed that ECOSTRESS LST and GOES LST showed overall great agreement during all the four tested time windows ( $r > 0.96$ , Figure S6 in Supporting Information S1), albeit with some discrepancies most likely due to the subgrid heterogeneity within the 2 km GOES pixels, as well as differences in instrument configurations and retrieval algorithms between the two products (summarized in Table 1).

#### 3.2.3. Data Input for the PT-JPL Model to Derive ET

To estimate ET using the PT-JPL model, ancillary data sets (Appendix B) are required to provide information on meteorology and surface properties. Table 2 lists all the required input data sets used in the operational ECOSTRESS ET product and in this study. ECOSTRESS LST was used to estimate the upward longwave radiation  $LW_{out}$  in both cases. For the other three radiation terms (downward/upward shortwave radiation, downward longwave radiation, Table B3), the operational ECOSTRESS ET product estimates them with an atmospheric radiative transfer model, that is, Forest Light Environmental Simulator (FLIES, Iwabuchi, 2006) with MODIS input for aerosols, clouds, and surface reflectances. For convenience, in this study, we calculated them with hourly data from the Global Modeling and Assimilation Office (GMAO) Modern-Era Retrospective analysis for Research and Applications, Version 2 (MERRA-2) reanalysis (longitude  $0.625^\circ \times$  latitude  $0.5^\circ$ , GMAO 2015a) and shortwave albedo from Landsat 8 (30 m, Liang, 2001, for the test domain centered at US-Seg) or from the Harmonized Landsat and Sentinel-2 (HLS) Version 2.0 (30 m, Masek et al., 2021a, 2021b, for the domain

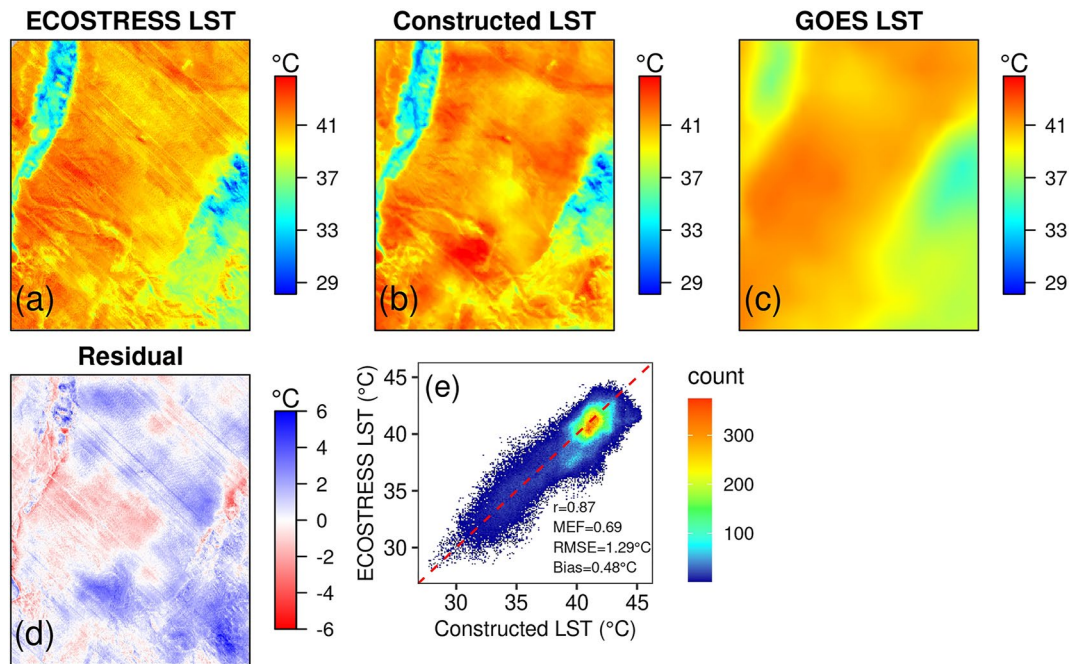


**Figure 5.** Evaluation of the diurnally resolved land surface temperature (LST) using the 14:56 (local time) overpass on 27 September 2020 as an example, for the test domain centered at US-Seg. (a) native ECOSTRESS LST; (b) constructed LST utilizing the leave-one-out approach (Section 2.4); (c) GOES LST interpolated spatially and temporally (Section 3.2.2); (d) prediction residuals, calculated as the difference between (b) and (a); and (e) scatterplot of (a) versus (b). The red dashed line represents the 1:1 line.

centered at US-ARM). Here HLS was selected because Landsat 8 reflectance was scarcely available during the selected time window in the test domain centered at US-ARM.

Air temperature and humidity, for the operational ECOSTRESS ET product, are diurnally interpolated from MODIS and will be updated with data from GEOS-FP (“forward-processing”) products in the future. In this study, we used the MERRA-2 hourly reanalysis (GMAO, 2015b) for a better characterization of diurnal meteorology despite its coarse resolution. We found that MERRA-2 Rn, Tair, VPD, and RH showed reasonable agreement with tower measurements at both US-Seg and US-ARM (Figures S2–S5 in Supporting Information S1), justifying our choice of the MERRA-2 reanalysis in deriving diurnal ET.

All the meteorological data from MERRA-2 were linearly interpolated to instantaneous timestamps from two nearby hourly timestamps. NDVI and albedo derived from Landsat 8 or HLS were linearly interpolated to each day. Variables from disparate sources have different spatial resolutions and therefore were spatially interpolated to ECOSTRESS resolution using bilinear interpolations.

## 4. Results

### 4.1. Spatial and Temporal Patterns of the Constructed Diurnal LST and ET for the Test Domain Centered at US-Seg

#### 4.1.1. The Constructed Diurnal LST

We first assessed the performance of the DTC model in capturing spatial patterns in the native ECOSTRESS LST. Specifically, we applied the DTC model to each ECOSTRESS pixel within the domain centered at US-Seg and generated spatially explicit (70 m resolution) and diurnally resolved LST mapping using the leave-one-out cross validation approach (Section 2.4), which in turn was evaluated against the native ECOSTRESS LST. Using the overpass of 14:56 (local time) on 27 September 2020 as an example, we found that our constructed LST (with the overpass excluded for parameter calibration) successfully reproduced the distinct spatial patterns (e.g., among different land cover types) in the native ECOSTRESS LST (Figures 5a, 5b and 5e,  $r = 0.87$ , MEF = 0.69 for this overpass). For example, forests (east), wetlands, and croplands (northwest) exhibited lower LST than

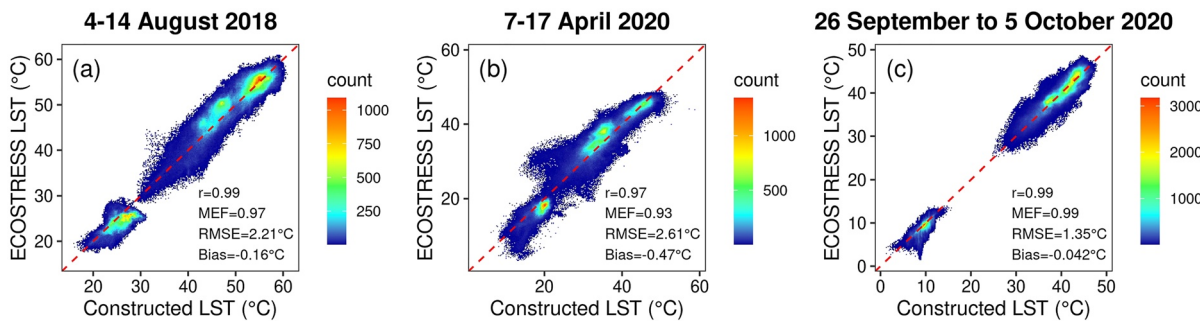


**Figure 6.** Comparison of the native ECOSTRESS land surface temperature (LST) (y axis) and the constructed LST (x axis) utilizing the leave-one-out approach including all the overpasses within each time window for all the pixels within the test domain centered at US-Seg: (a) 4–14 August 2018; (b) 7–17 April 2020; and (c) 26 September–5 October 2020. Colors indicate density of scatter counts, from low (blue) to high (red). The red dashed line represents the 1:1 line.

shrublands and grasslands (center). The prediction residuals were overall minimal (Figure 5e, RMSE = 1.48°C, Bias = 0.48°C for this overpass), despite somewhat spatial dependence (Figure 5d). Importantly, although the coarse resolution GOES LST was extensively used in the DTC model parameter fitting, the constructed ECOSTRESS LST was capable of revealing substantially more fine spatial details than possibly by GOES LST (Figure 5c), demonstrating the added value of fine resolution ECOSTRESS LST enabled by our framework.

Expanding such evaluation to all ECOSTRESS overpasses (available only on clear-sky conditions) for each time window (Figure 6), we further demonstrated the capability of the DTC model in reliably reproducing the spatio-temporal pattern of the native ECOSTRESS LST that was diurnally sampled, even on days when ECOSTRESS observations are not available ( $r > 0.97$ , MEF > 0.93, RMSE = 1.35–2.61°C, |Bias| < 0.5°C). As we hypothesized in Section 3.1, the constructed LST showed greater consistency with the native ECOSTRESS LST in the third window (Figure 6c) than the first two windows (Figures 6a and 6b), possibly due to impact of the occurrence of rainy/cloudy conditions (that decrease the availability of ECOSTRESS and GOES measurements employed for the DTC model fitting) as well as the lower consistency between ECOSTRESS and GOES in the first two windows (Figure S6 in Supporting Information S1).

We then evaluated the capability of DTC in reproducing the temporal dynamics in the in situ LST at the local US-Seg tower. The constructed LST time series showed strong agreement in diurnal variations with the in situ LST across all the three phenological periods for nonrainy days ( $r = 0.96$ –0.98, MEF = 0.89–0.96, RMSE = 2.36–3.44°C, |Bias| = 0.26–0.82°C, Figures 7 and 8). The constructed LST also captured the day-to-day variation in the in situ LST, for example, lower LST on 28 September 2020 compared to adjacent days (Figure 7c). The first two time windows showed slightly degraded performance (i.e., lower  $r$  and MEF, higher RMSE and |Bias|, Figures 8a and 8b) compared to the third one (Figure 8c), possibly due to the occurrence of clouds and rainy events (despite that rainy days were excluded from the statistical analysis). We further evaluated the performance of the DTC model at this site separately for clear-sky and cloudy conditions (Section 3.1) during the daytime (Table 3). As expected, the constructed LST showed lower consistency with tower LST under cloudy conditions (RMSE = 2.35–6.10°C, |Bias| = 0.79–2.48°C), compared to clear-sky conditions (RMSE = 2.44–3.72°C, |Bias| = 0.30–1.95°C). The large RMSE and |Bias| on cloudy conditions are mostly due to the mismatch on 6 and 12 August 2018 and 12 April 2020, when LST deviated from the prescribed clear-sky diurnal shape of the DTC model and therefore led to a clear-sky bias. In addition, RMSE of clear-sky LST was slightly larger in the first two windows than that in the third window, likely due to overall lower availability of satellite observations and lower consistency between GOES and ECOSTRESS (Figure S6 in Supporting Information S1) during the whole time window.

The above assessments at both landscape and site scales have demonstrated that the DTC model can effectively construct the full diurnal cycle of LST from sporadic ECOSTRESS measurements under clear-sky conditions. The full hourly time series of LST mapping in this test domain is animated in Figure S10a in Supporting Information S1, using the 26 September–5 October 2020 window as an example.

Note that with the occurrence of clouds or rain events, the performance of the DTC model could be degraded because under these conditions (a) LST variation can deviate from the prescribed diurnal shape and/or (b) ECOSTRESS and GOES observations are less available for model fitting. These issues are thoroughly discussed in Sections 5.3 and 5.5.

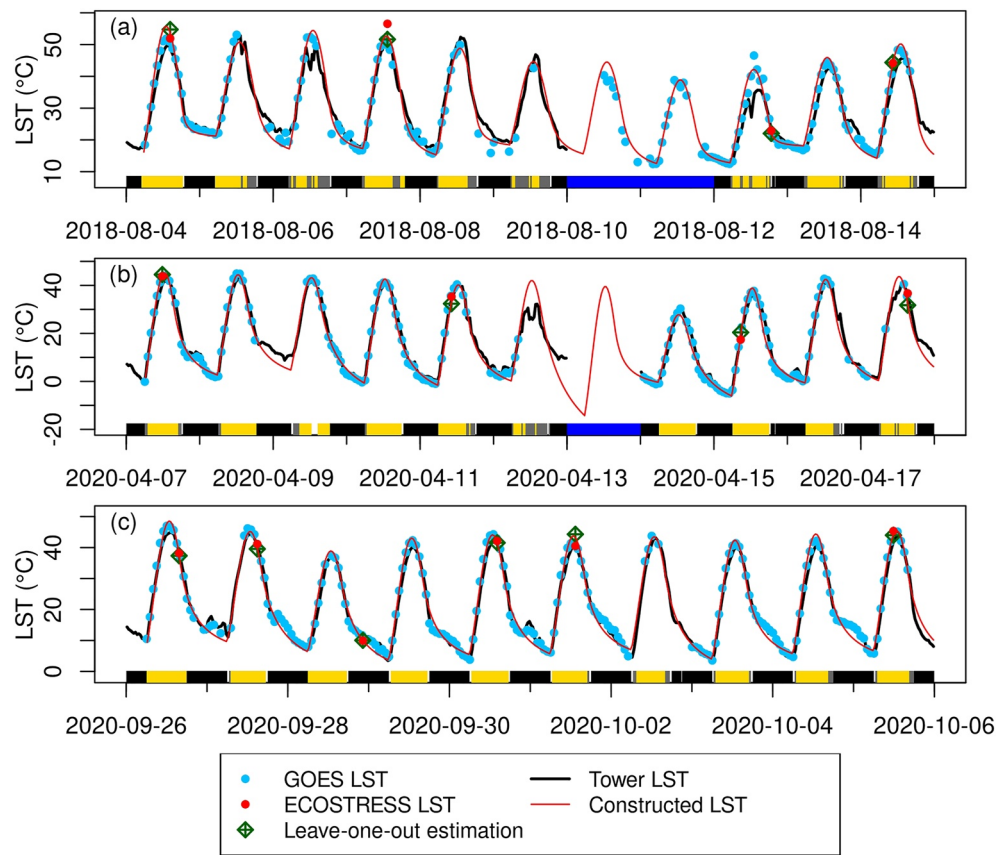


**Figure 7.** The constructed diurnal land surface temperature (LST) at US-Seg during the three time windows (corresponding to three distinct phenological stages): (a) 4–14 August 2018; (b) 7–17 April 2020; and (c) 26 September–5 October 2020. GOES and ECOSTRESS LST observations are marked in light blue and red dots, respectively; leave-one-out estimation (Section 2.4) for each ECOSTRESS overpass is marked as dark green diamond plus; the constructed LST fitted with all available ECOSTRESS overpasses is represented with a red line, while tower LST is drawn as a black line. Rainy days (blue) as well as clear-sky (yellow, daytime only), cloudy-sky (gray, daytime only), nighttime (black), and unknown (white, due to missing in situ data) periods of nonrainy days are marked at the bottom of each panel.

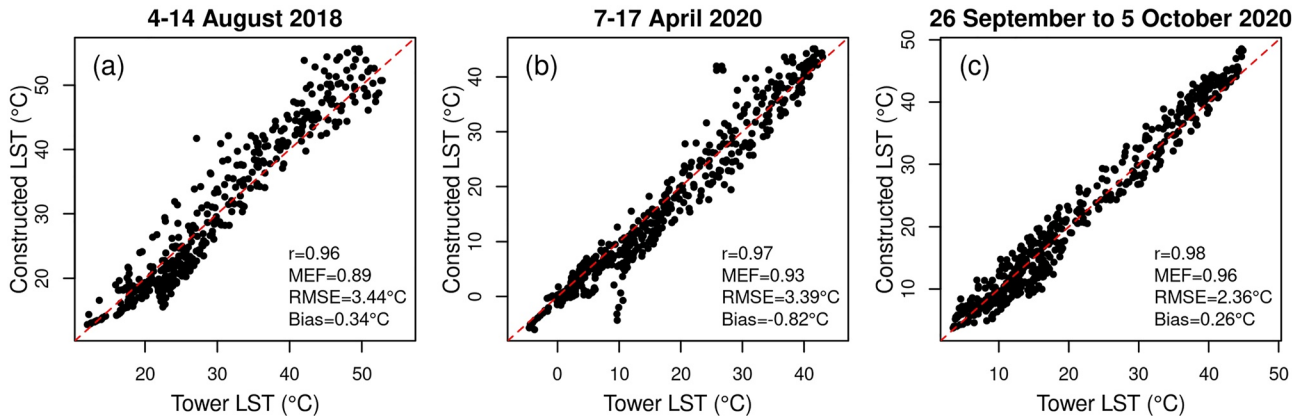


**Figure 8.** Comparison of the constructed diurnal land surface temperature (LST) with the in situ LST at US-Seg during the three time windows (corresponding to three distinct phenological stages): (a) 4–14 August 2018; (b) 7–17 April 2020; and (c) 26 September–5 October 2020. Rainy days are excluded from plotting and statistical analysis.

**Table 3**

*Comparison of the Constructed Diurnal LST With the In Situ LST at US-Seg, Separately for Clear-Sky and Cloudy Conditions During the Daytime*

4–14 August 2018		7–17 April 2020		26 September–5 October 2020	
Clear (n = 187)	Cloudy (n = 102)	Clear (n = 198)	Cloudy (n = 65)	Clear (n = 208)	Cloudy (n = 17)
RMSE (°C)	3.72	4.22	2.80	6.10	2.44
Bias (°C)	1.95	2.58	-0.30	2.48	1.31

#### 4.1.2. The Constructed Diurnal ET

We subsequently evaluated the performance of the PT-JPL model in constructing diurnal ET. Similar to LST, we first compared the native ECOSTRESS ET and the constructed ET calculated with leave-one-out LST estimation to evaluate their spatial consistency. Using the overpass of 13:20 (local time) on 7 August 2018 as an example, we demonstrated that the constructed ET (Figure 9b) successfully characterized the distinct spatial patterns (e.g., among different land covers) in the native ECOSTRESS ET (Figure 9a): Highest ET in croplands and wetlands (northeast), lowest in shrublands/grasslands (center), and moderate in forests (east). This was also evidenced by high  $r$  (0.93) and MEF (0.83) for this overpass (Figure 9d). However, we observed some differences between our constructed ET and the native ECOSTRESS ET, for example, underestimation for croplands/wetlands and shrublands/grasslands, and overestimation for forests (Figure 9c). Such landcover-dependent bias was likely due to the differences in the reflectance data sets employed in this study and the ECOSTRESS operational ET product (Table 2); additionally, differences in the meteorological data sets (provided at a coarser resolution) can also result in an overall magnitude offset in this test domain.

To disentangle whether such ET discrepancy arose from the differences in the input ancillary data sets between this study and the ECOSTRESS operational product (summarized in Table 2), we compared our constructed ET with that calculated from the native ECOSTRESS LST but using the same ancillary data sets (i.e., reflectance and meteorological variables) as in this study, denoted as ECOSTRESS ET\* (Figure 9e). Much more pronounced agreement was achieved ( $r = 1.00$ , MEF = 1.00, RMSE =  $3.87 \text{ W m}^{-2}$ , Bias =  $2.07 \text{ W m}^{-2}$ ; Figures 9f and 9g) for the overpass. This indicated that the discrepancies between ECOSTRESS ET and the constructed ET mainly

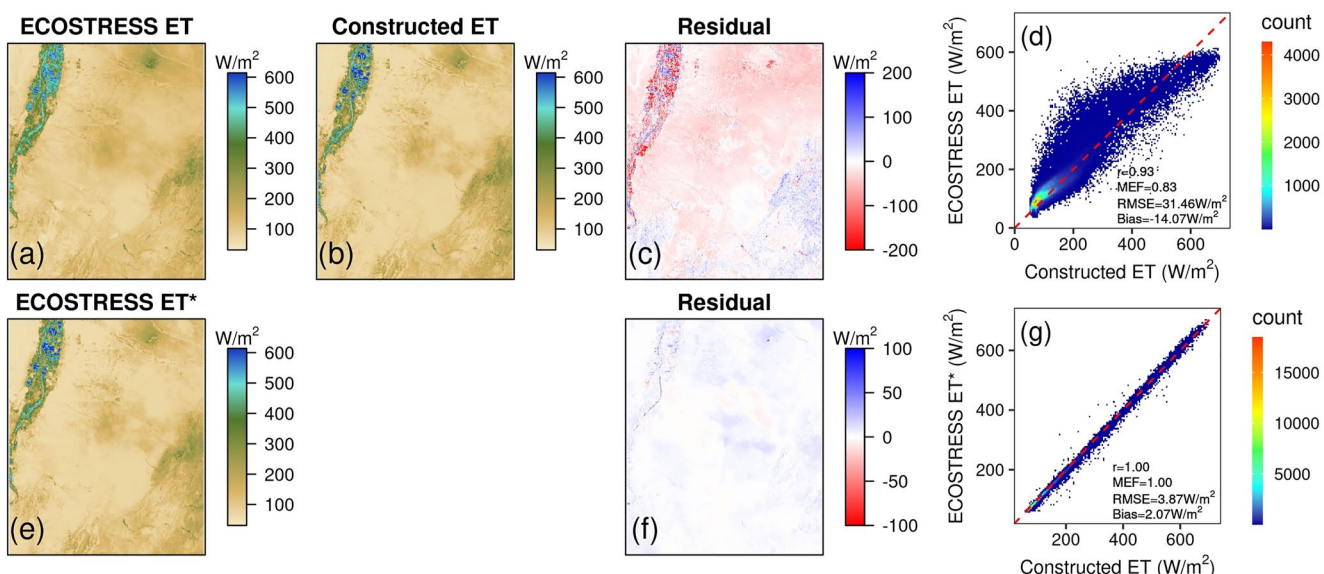


**Figure 9.** Comparison between ECOSTRESS evapotranspiration (ET) and the constructed ET for the overpass of 13:20 (local time) on 7 August 2018, as an example. (a) native ECOSTRESS ET; (b) constructed ET, calculated from leave-one-out LST approach; (c) prediction residual calculated as the difference between (b) and (a); (d) scatterplot of (a) (y-axis) versus (b) (x-axis); (e) ECOSTRESS ET\*, calculated from the native ECOSTRESS LST using the same ancillary data sets as were used in this study, for example, in (b); (f) prediction residual calculated as the difference between (b) and (e); and (g) scatterplot of (e) (y-axis) versus (b) (x-axis). The red dashed line is 1:1 line.

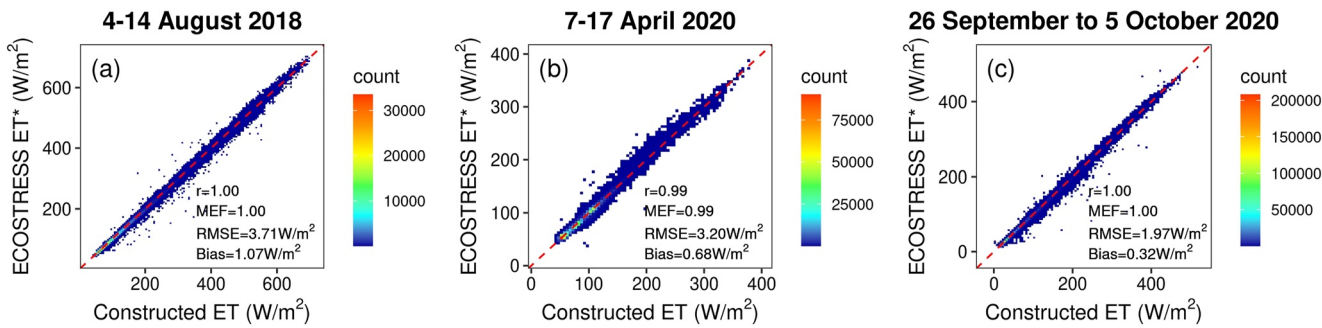


**Figure 10.** Comparison between ECOSTRESS ET\* (y axis) and the constructed evapotranspiration (ET) (x axis) pooled from all the pixels and all the overpasses of each time window: (a) 4–14 August 2018; (b) 7–17 April 2020; and (c) 26 September–5 October 2020. Different colors indicate density of scatter counts, from low (blue) to high (red). The red dashed line is 1:1 line.

resulted from the differences in the input ancillary data sets, compared to the differences between ECOSTRESS LST and the constructed LST.

Furthermore, such consistency was observed for all the three time windows (Figure 10), with  $r$  and MEF close to 1, and RMSE and bias nearly 0 W m<sup>-2</sup>. The first two time windows with occurrence of clouds and rain events showed slightly degraded performance (note that the evaluation was conducted only for clear-sky overpasses), albeit very minimal, mostly due to the error propagation from the leave-one-out LST estimation (Figure 6). The full hourly time series of ET mapping in this test domain is animated in Figure S10b in Supporting Information S1, using the 26 September–5 October 2020 window as an example.

Next, we compared the constructed ET with independent ET flux measured at US-Seg. Notably, the constructed ET and ECOSTRESS ET exhibited an overall positive bias compared to the in situ ET (Figure 11). We performed sensitivity analyses and found that better agreement could be achieved for all the three periods (Figure 11) if multiplying the soil moisture constraint  $f_{SM}$  by a scaling factor of 0.5 in our constructed ET (Equation 14, in comparison to the corresponding equation in Table B2).

$$f_{SM} = 0.5RH^{VPD} \quad (14)$$

With  $f_{SM}$  modified, the constructed ET showed overall agreement with tower ET in general ( $r = 0.47$ – $0.82$ ,  $|Bias| = 1.47$ – $6.41$  W m<sup>-2</sup>, Figure 12). Further, the constructed ET reasonably reproduced the rainfall-led ET increase as observed in the in situ ET (i.e., 9 vs. 12 August 2018 and 12 vs. 15 April 2020). Lower  $r$  and MEF observed in the third window, despite lower RMSE and Bias, were primarily due to smaller diurnal variation of ET (therefore measurement noise and prediction residuals had a larger impact on the calculation of  $r$  and MEF). High RMSE (~40% of the daytime mean of the in situ ET in Figure 11) in the first two time windows, however, was likely due to the occurrence of rain events. Although rainy days were already excluded for comparison due to high uncertainty in the in situ flux measurements of ET, the complex meteorological dynamics might still affect the ET modeling before and after the rain events. For example, on 14 April 2020 after the rain event, there was a huge instant increase in tower ET (Figure 11b) possibly from evaporation from canopy interception and soil, which was not captured by the constructed ET. Although VPD was lower and RH was higher than normal (Figure S3 in Supporting Information S1), they did not lead to the rapid surge of ET (as large as observed) using the PT-JPL model. During 6–9 August 2018 before the rain event, tower ET showed a decreasing pattern as the soil dried out (Figure S7 in Supporting Information S1), which however was not captured by the constructed ET either. This soil drying could not be detected in VPD and RH either from MERRA-2 or the tower measurements (Figure S2 in Supporting Information S1). As VPD and RH were used to formulate  $f_{SM}$  and  $f_{wet}$ , two critical constraint factors to characterize soil moisture and wetness in the PT-JPL model, the decoupling between VPD or RH and the soil drying during this time period could influence the constructed ET, which did not exhibit a gradual decrease. The above findings suggest that a better proxy for soil water content or better formulation of soil moisture constraint may be needed for the PT-JPL model (Purdy et al., 2018). This issue is further discussed in Section 5.4.

Also note that the constructed ET was much smoother while the in situ ET showed more fluctuations. The discrepancy between MERRA-2 and tower meteorological data might play a role, as MERRA-2 may not well

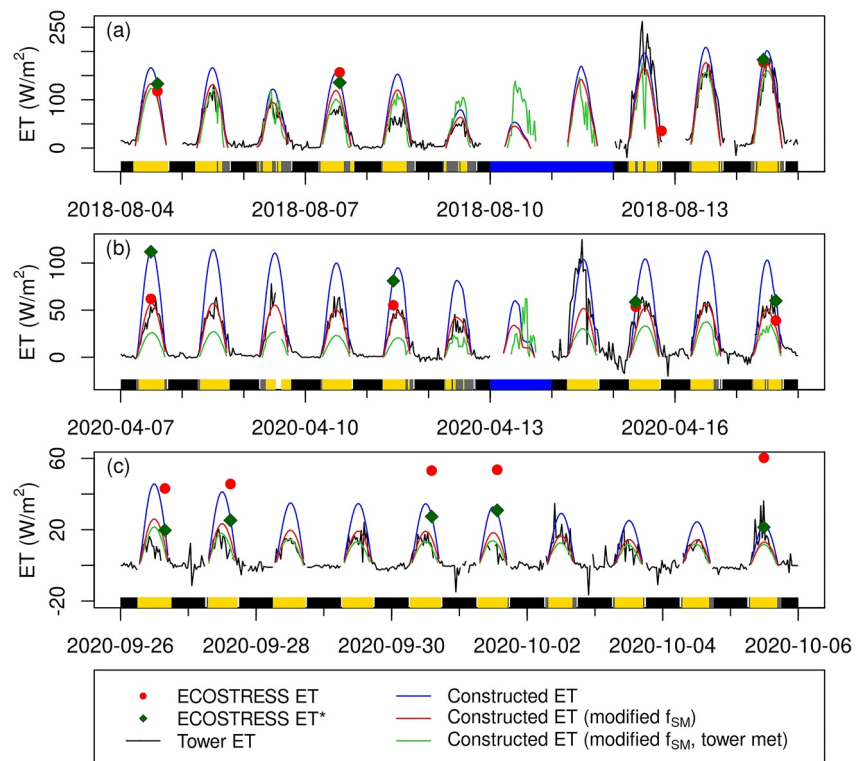


**Figure 11.** Comparison of the constructed ECOSTRESS evapotranspiration (ET) and in situ ET at US-Seg during (a) 4–14 August 2018; (b) 7–17 April 2020; and (c) 26 September–5 October 2020. The constructed ET (using MERRA-2 reanalysis as meteorological input) without and with  $f_{SM}$  modified (by multiplying a factor of 0.5) are denoted as blue and red curves, respectively; the constructed ET (using tower data as meteorological input) with  $f_{SM}$  modified is drawn in green; tower ET is drawn in black. ECOSTRESS ET observations and ECOSTRESS ET\* are marked in red dots and dark green diamonds. Rainy days (blue) as well as clear-sky (yellow, daytime only), cloudy-sky (gray, daytime only), nighttime (black), and unknown (white, due to missing in situ data) periods of nonrainy days are marked at the bottom of each panel. Only daytime ET was used for analysis as ET is set to zero when  $R_n$  is negative in the PT-JPL model.

capture the rapid micrometeorological fluctuations. A test run with in situ meteorological measurements at the tower as input indeed showed an improved agreement with tower ET in terms of the diurnal fluctuations (e.g., 12 and 17 April 2020, Figure 11). In addition, in situ ET itself may have large measurement noise and uncertainty (e.g., Richardson et al., 2006), which can lead to considerable fluctuations in ET measurements (e.g., 10 April

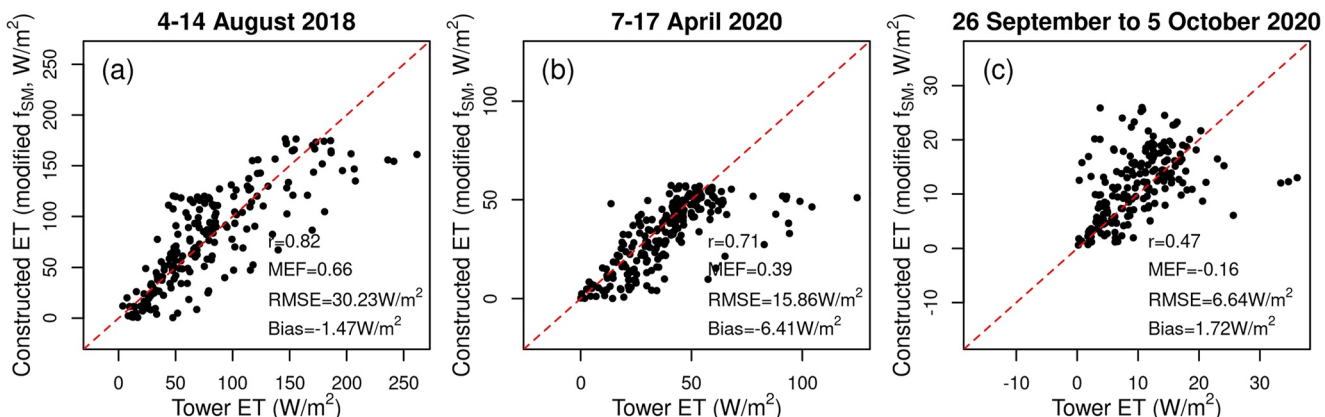


**Figure 12.** Comparison between the constructed diurnal evapotranspiration (ET) (with  $f_{SM}$  modified) with tower ET at US-Seg during the three time windows (corresponding to three distinct phenological stages): (a) 4–14 August 2018; (b) 7–17 April 2020; and (c) 26 September–5 October 2020. Rainy days are excluded from plotting and statistical analysis.

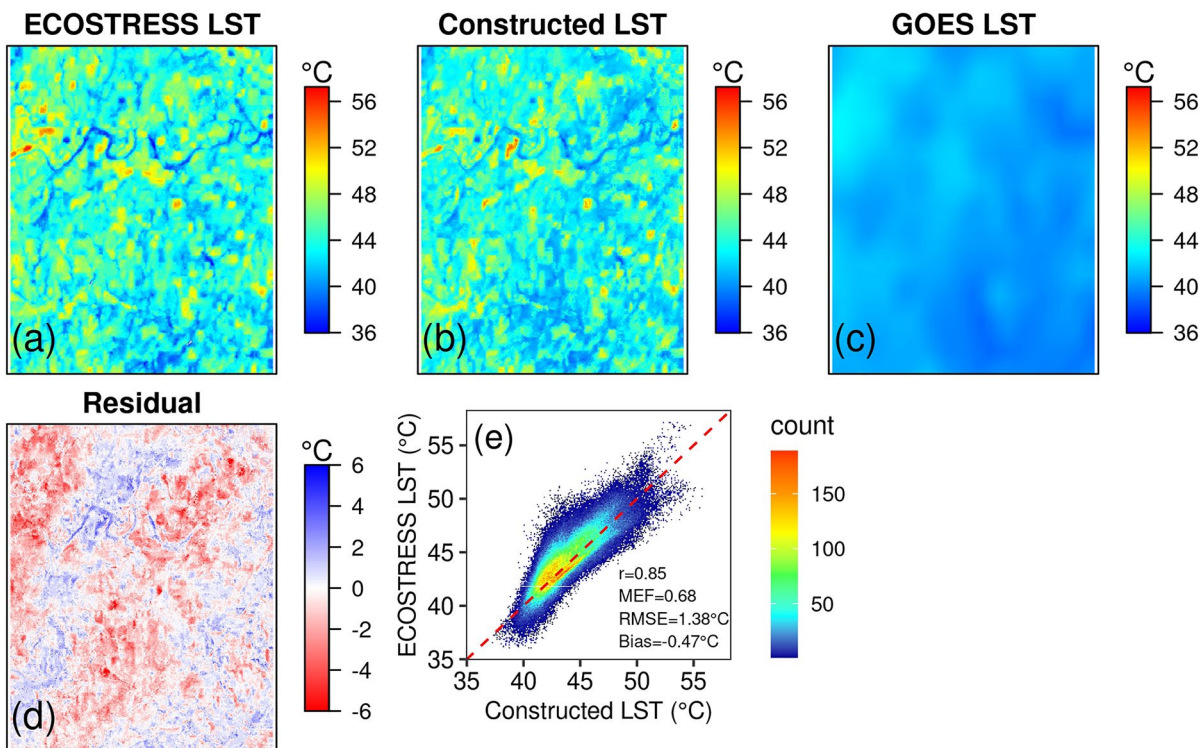


**Figure 13.** Comparison between the native ECOSTRESS land surface temperature (LST) and the constructed LST for a heterogeneous landscape centered at US-ARM during the overpass of 14:24 in local time on 18 June 2021, as an example, similar to Figure 5. (a) native ECOSTRESS LST observations; (b) constructed LST using the leave-one-out approach (Section 2.4); (c) GOES LST interpolated spatially and temporally (Section 3.2.2); (d) prediction residuals calculated as the difference between (b) and (a); and (e) scatterplot of (a) versus (b). The red dashed line is 1:1 line.

2020, Figure 11b) but cannot be simulated with a model (which is noise free), even driven by in situ meteorological data sets (which are much less noisy than flux measurements, Figure S3 in Supporting Information S1).

#### 4.2. Spatial and Temporal Patterns of the Constructed Diurnal LST and ET for the Test Domain Centered at US-ARM

To demonstrate the scalability and effectiveness of our framework in heterogeneous landscapes, we applied it to a test domain centered at US-ARM, with diverse vegetation types (e.g., winter wheat, soybean, and grass). Our results revealed similar performance as compared to US-Seg. Specifically, the constructed LST (based on the leave-one-out approach, Figure 13b) considerably captured the fine spatial variations (e.g., crop fields) of the native ECOSTRESS LST (Figure 13a,  $r = 0.85$ , MEF = 0.68, using the overpass of 14:24 on 18 June 2021 as an example), which cannot be resolved by GOES LST (Figure 13c). The residual was somewhat clustered but overall minimal (Figure 13d, RMSE = 1.38°C, Bias = -0.47°C).

The constructed ET (calculated with leave-one-out LST estimation) clearly resolved the distinct spatial patterns (e.g., among different crop types), in high agreement with ECOSTRESS ET\* (calculated with the native ECOSTRESS LST and the same ancillary data sets as those for the constructed ET) (Figure 14,  $r = 0.98$ , MEF = 0.95, RMSE = 12.48 W m<sup>-2</sup>, Bias = 1.63 W m<sup>-2</sup> for the single overpass).

Expanding the above evaluation to all the overpasses, our framework again demonstrated its capability in reproducing the spatiotemporal pattern of ECOSTRESS LST (Figure 15a,  $r = 0.98$ , MEF = 0.96, RMSE = 1.74°C, Bias = -0.077°C) and ET\* (Figure 15b,  $r = 1.00$ , MEF = 0.99, RMSE = 6.77 W m<sup>-2</sup>, Bias = 0.37 W m<sup>-2</sup>).

We also compared the constructed LST and ET with the in situ measurements. The constructed LST successfully captured the diurnal variation of the in situ LST (Figure 16a,  $r = 0.99$ , MEF = 0.91, RMSE = 2.17°C, Bias = 1.47°C), despite some overestimation during the midday, which was likely caused by the positive bias of the native ECOSTRESS LST during the midday overpasses on 17 and 18 June 2021. Similar to US-Seg, we also found an overestimation in both ECOSTRESS ET and our constructed ET, relative to the in situ ET

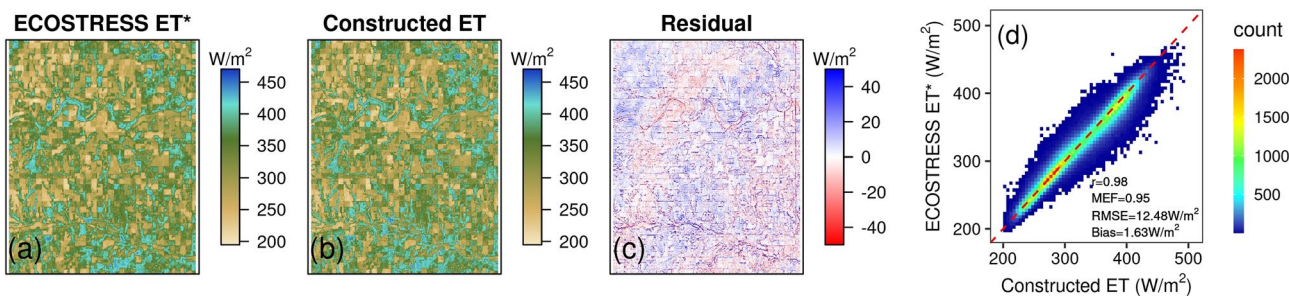


**Figure 14.** Comparison between ECOSTRESS ET\* and the constructed ET for a heterogeneous landscape centered at US-ARM during the overpass of 14:24 in local time on 18 June 2021, as an example, similar to Figure 9. (a) ECOSTRESS ET\*; (b) constructed ET; (c) prediction residual calculated as the difference between (b) and (a); and (d) scatterplot of (a) (y-axis) versus (b) (x-axis). The red dashed line is 1:1 line.

(Figure 16b). After similarly modifying the constraint factor  $f_{SM}$  by multiplying a factor of 0.5, the mismatch between constructed ET and tower ET was greatly reduced ( $r = 0.80$ , MEF = 0.15, RMSE =  $46.57 \text{ W m}^{-2}$ , Bias =  $29.38 \text{ W m}^{-2}$  with  $f_{SM}$  modified). Note that here, we chose 0.5 as the factor to be consistent with the analysis at US-Seg. If further calibrated, smaller RMSE and Bias relative to the in situ ET could be possibly achieved.

The results given above have demonstrated that our framework is applicable to heterogeneous landscapes as well, albeit that the PT-JPL model may require soil moisture information as input and calibration of the parameters at the local scale to better characterize the soil moisture constraint on ET.

## 5. Discussion

In this study, we developed the first framework to resolve the clear-sky continuous diurnal cycle of LST and ET of ECOSTRESS at 70 m resolution and examined its performance for both homogeneous and heterogeneous landscapes. Using the leave-one-out cross validation approach, we have demonstrated that our developed framework is capable of reproducing the spatiotemporal pattern of the native ECOSTRESS LST and ET (if using the same meteorological and reflectance as ancillary input) in both landscapes. Great agreement was achieved for all land cover types (i.e., shrublands, grasslands, croplands, wetlands, and forests) in our study domains. Note that our leave-one-out validation approach is already highly conservative for evaluating the model performance in this case because withdrawing one sample can substantially enlarge the temporal gaps by a factor of two and could considerably influence the model fitting given the limited ECOSTRESS sampling frequency. Agreement with independent in situ LST and ET measurements similarly reveals the effectiveness of our developed framework, albeit to a lesser degree for ET. This is nevertheless expected, as ET flux is more dynamic and regulated by more factors, therefore more challenging to model, compared to LST. Higher measurement noise in ET (a flux variable) than LST may also explain the reduced performance in the constructed ET relative to LST.

In the following, we further discuss how subgrid heterogeneity within the coarse GOES pixels can be effectively resolved in our framework, which is one of the innovations of this study (Section 5.1). Then we highlight the

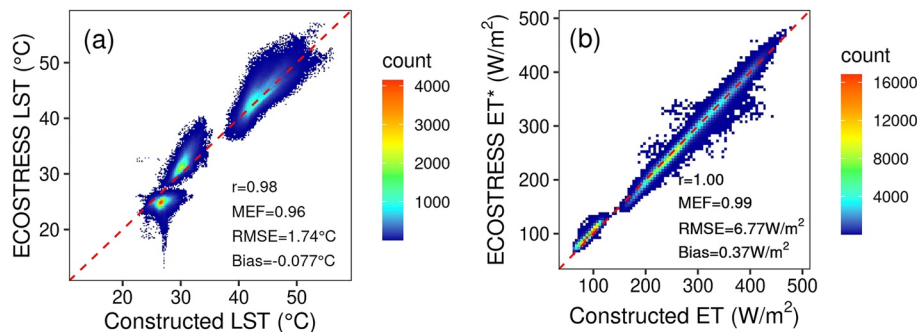


**Figure 15.** Comparison of (a) the native ECOSTRESS land surface temperature (LST) (y axis) and the constructed LST (x axis) and (b) ECOSTRESS ET\* (y axis) and the constructed ET (x axis), pooled together from all the pixels and all the overpasses during 15–19 June 2021 for the domain centered at US-ARM, similar to Figures 6 and 10.

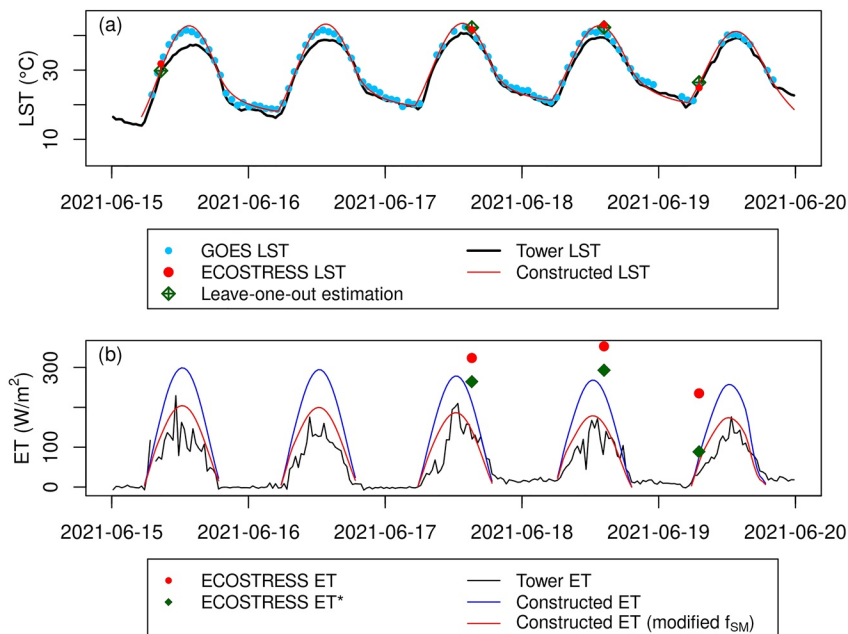


**Figure 16.** Evaluation of the constructed diurnal land surface temperature (LST) and evapotranspiration (ET) at US-ARM during 15–19 June 2021, similar to Figures 7 and 11.

advantages of our developed framework in constructing diurnal ET from sporadic ET measurements, by explicitly comparing the diurnal ET estimates derived from (a) the framework developed in this study and (b) linearly scaling with incoming radiation. Following that, we discuss several caveats and possible applications in this study, which warrant continued future research (Sections 5.3, 5.4, 5.5, 5.6, 5.7, 5.8).

### 5.1. Resolving the Subgrid Heterogeneity Within the Coarse GOES Pixels

In this study, we constructed the diurnal cycle of LST at high spatial resolution (70 m) with sporadic ECOSTRESS diurnal samplings utilizing hourly GOES observations at low spatial resolution (2 km). Specifically, GOES observations were utilized to fit the time-related DTC parameters and further to constrain the day-to-day LST variations; GOES and ECOSTRESS observations were altogether utilized to fit the temperature-related DTC parameters (Section 2.2). Although GOES LST was extensively used in the DTC model fitting, our results have shown that the subgrid heterogeneity within the coarse GOES pixels can be effectively resolved in our developed framework (Figures 5 and 13).

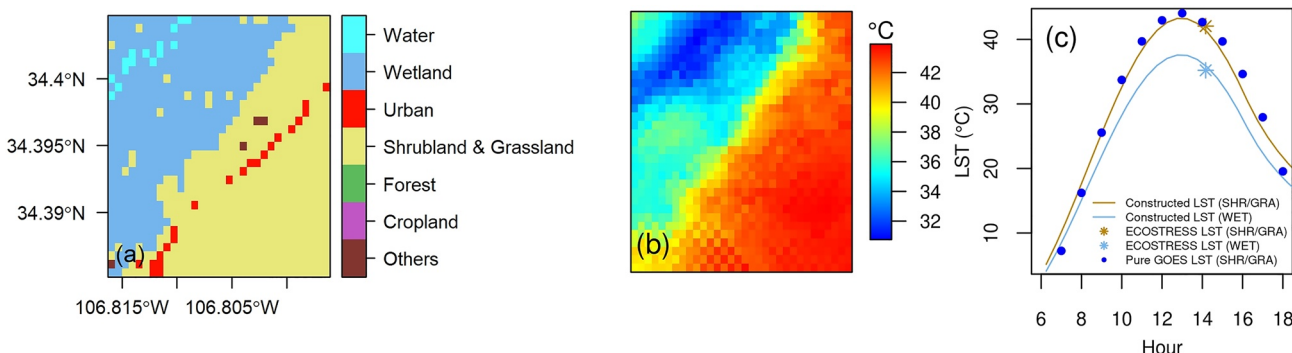


**Figure 17.** An example of how the diurnal temperature cycle (DTC) model effectively resolves the diurnal cycle of 70 m ECOSTRESS pixels with distinct land cover types within a coarse 2 km GOES pixel (106.8062°W, 34.39493°N). (a) Land cover map within the selected GOES pixel (marked in Figure 4a); (b) ECOSTRESS LST on 30 September 2020, 14:10 (local time); and (c) The constructed land surface temperature (LST) (line) and the native ECOSTRESS LST (square cross) averaged for shrubland and grassland pixels (brown) and wetland pixels (light blue) in (a), respectively, on 30 September 2020. GOES LST of pure pixels with 100% shrubland and grassland coverage is plotted (blue dots) for reference.

To demonstrate this, we conducted a further test. We selected a single 2 km GOES pixel (106.8062°W, 34.39493°N, marked in Figure 4a) with distinct land cover types (i.e., endmembers) inside (Figures 17a and 17b). The tested GOES pixel is mostly covered by shrublands/grasslands and wetlands, with approximately equal fractional coverage. Our results showed that DTC successfully revealed the distinct magnitudes and diurnal cycles of two land cover types within the coarse GOES pixel, both of which matched well with the original ECOSTRESS LST measurements during the overpass (Figure 17c). To verify the validity of the constructed LST diurnal cycle at fine ECOSTRESS pixels, we extracted the diurnal shapes of LST from pure GOES pixels (i.e., with 100% coverage of the same land cover) from the whole tested spatial domain (Figure 4a), as a reference, assuming that the fine ECOSTRESS pixels and coarse pure GOES pixels share similar thermal properties and diurnal cycles. The constructed diurnal cycle of shrublands/grasslands at fine ECOSTRESS pixels followed closely with that of the pure GOES pixels (Figure 17c). The diurnal cycle of wetlands is not included here for analyses because there is no GOES pixel with >75% wetland coverage that can be deemed as a pure pixel for cross comparison. This result has further demonstrated that our framework is able to effectively resolve the diurnal cycle for different endmembers in a coarse GOES pixel, despite the subgrid heterogeneity within coarse GOES pixels and instrument discrepancies between GOES and ECOSTRESS.

### 5.2. Comparison With Daily ET Estimate Scaled From $SW_{in}$

Daily ET estimate is usually derived by scaling instantaneous ET (inferred from satellite thermal measurements during the overpass time) with solar radiation (e.g., Anderson et al., 2021; Cammalleri et al., 2014; Fisher & ECOSTRESS algorithm development team., 2015), which assumes a linear scaling between ET and  $SW_{in}$  or  $R_n$ . However, although such scaling can account for the first-order diurnal variation of ET, other abiotic and biotic conditions (e.g., atmospheric dryness and stomatal closure) are not considered, which may lead to varying degree of bias (Cammalleri et al., 2014). In this study, we utilized the PT-JPL model to resolve the diurnal cycle of ET driven by diurnal LST and other variables (e.g., meteorological forcings and vegetation properties), which may help improve the diurnal characterization and daily estimation of ET.

In this section, we explicitly compared the diurnal and daily ET estimate from two approaches on days when ECOSTRESS observations were available: (a) ET constructed with our developed framework, that is, constructed ET and (b) ET scaled from instantaneous ET (the constructed ET at ECOSTRESS overpass time) with diurnal  $SW_{in}$  from MERRA-2 (Equation 15), that is, scaled ET.

$$ET(t) = \frac{ET(t_{overpass})}{SW_{in}(t_{overpass})} \times SW_{in}(t) \quad (15)$$

where  $ET(t_{overpass})$  and  $SW_{in}(t_{overpass})$  are instantaneous ET (from the constructed ET) and  $SW_{in}$  (from MERRA-2) at ECOSTRESS overpass time  $t_{overpass}$ ;  $ET(t)$  is the scaled diurnal ET with diurnal  $SW_{in}(t)$  (from MERRA-2) at time  $t$ . Here  $SW_{in}$  was selected because it has been demonstrated as the best reference variable among others (e.g., top-of-atmosphere radiance) for diurnal ET scaling (Cammalleri et al., 2014). Note that the constructed ET was used in Equation 15 instead of the native ECOSTRESS ET, to exclude the confounding impact from the discrepancies in the input ancillary data sets (Table 2).

We found that scaling with  $SW_{in}$  can lead to a discrepancy up to 22% in the daily ET, compared to the constructed ET (Figure 18). Notably, the degree of discrepancy varied across in time (different times of a day and across days, Figure 18) and space (Figure 19). For example, there was a large discrepancy in the midday when ECOSTRESS overpass time was in the early morning; our constructed ET showed a higher consistency with tower ET in the daily peak value (Figures 18f and 18o). Besides, the constructed ET showed a lower estimate than the scaled ET in the afternoons during the peak growing season (Figures 18a–18c) when VPD was as high as 4.5 kPa (Figure S2 in Supporting Information S1). Such diurnal hysteresis possibly due to atmospheric dryness and stomatal closure could not be captured by the scaled ET. This is expected, because  $SW_{in}$  is often diurnally symmetrical under clear days and only serves as first order approximation for diurnal ET variations. Note that considering the discrepancies between the native ECOSTRESS ET and the tower ET along with high measurement noise in the tower ET, we here mainly focus on the differences between the two scaling approaches (i.e., black and red dots in Figure 18).

Furthermore, we examined the spatial distribution of the differences between the scaled ET and the constructed ET, using 4 August 2018 as an example, for the test domain centered at US-Seg (Figure 19). We found that although the

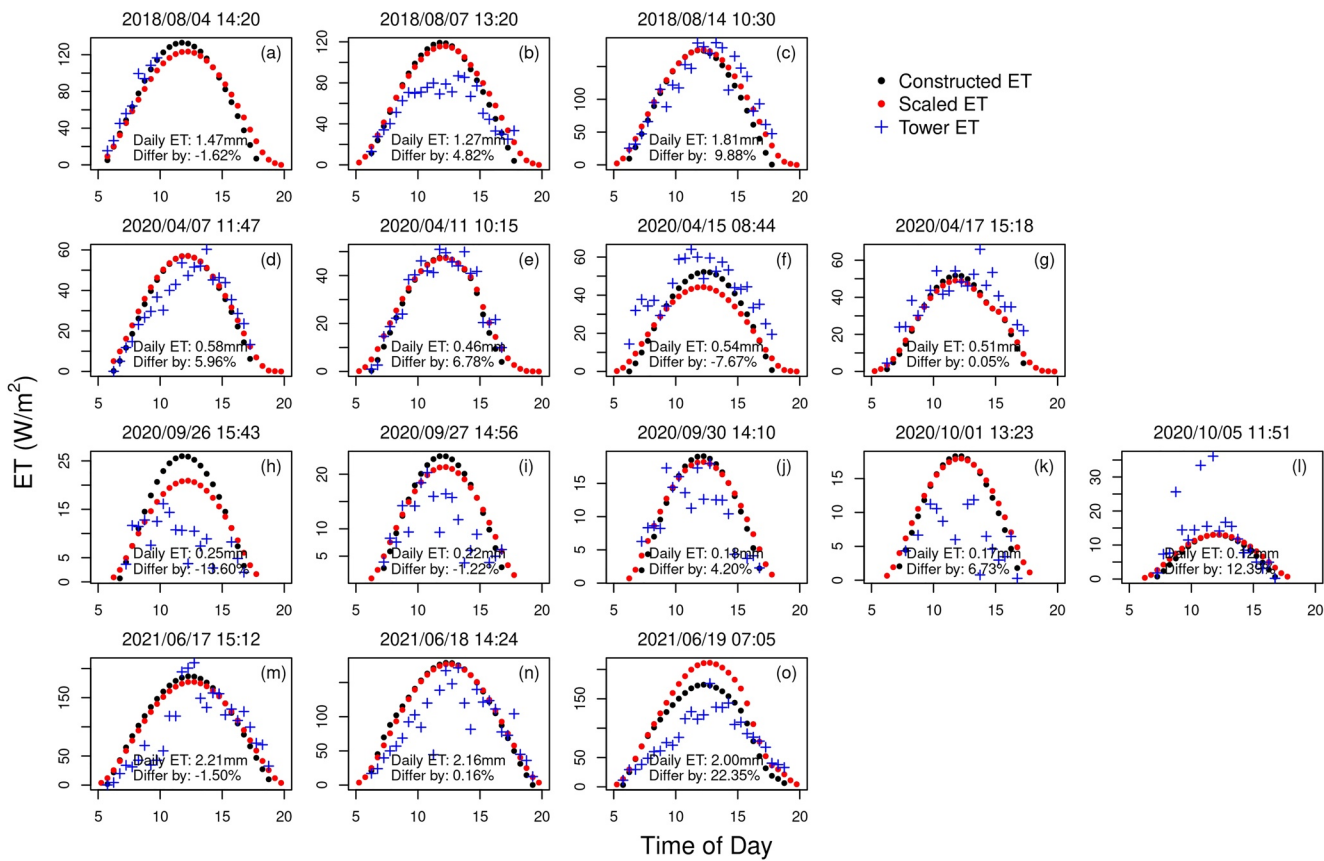


**Figure 18.** Comparison between the constructed evapotranspiration (ET) (generated from our developed framework, with  $f_{SM}$  modified, black dots) and the scaled ET (based on the assumption of linear relationship with diurnal SW<sub>in</sub> (Equation 15), red dots) on days when ECOSTRESS observations are available. Tower ET is plotted with blue cross. The four rows show the four tested period, respectively, with ECOSTRESS overpass time annotated above each panel. The overpass at 18:44 local time, 12 August 2018 is not shown because the constructed ET was zero because of negative  $R_n$ . Daily ET values in the text was calculated as total constructed ET during the daytime, in the unit of mm. The relative difference in daily ET was calculated as (scaled ET – constructed ET)/constructed ET × 100%.

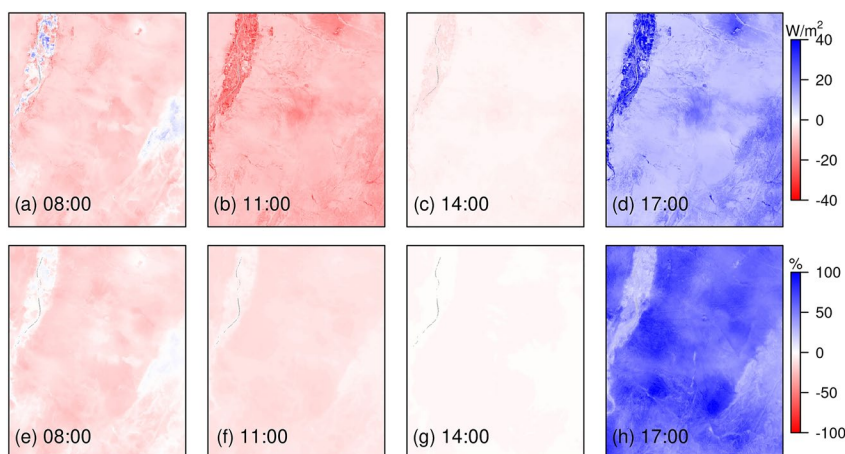


**Figure 19.** Spatial maps of the (a–d) absolute and (e–h) relative differences between the scaled evapotranspiration (ET) and the constructed ET for the test domain centered at US-Seg, at (a, e) 08:00, (b, f) 11:00, (c, g) 14:00, and (d, h) 17:00 local time, using 4 August 2018 as an example. The ECOSTRESS overpass time was 14:20 that day. The relative difference was calculated as (scaled ET–constructed ET)/constructed ET × 100%, similar to Figure 18.

difference was minimal when the timestamp was close to the ECOSTRESS overpass time, that is, 14:20 local time on that day (Figures 19c and 19g), there could be large discrepancies for other timestamps. For example, compared to the constructed ET, the scaled ET had 10% negative bias in the morning (08:00, Figures 19a and 19b; 11:00, 19e and 19f) and up to 50% positive bias in the afternoon (17:00, Figures 19d and 19h), compared to the constructed ET. This temporal pattern of discrepancy was consistent with our evaluation at the site location (Figure 18a). More importantly, such discrepancies vary not only with time of day but also with biome types and environmental conditions. These results indicate that the linear scaling with  $SW_{in}$  is not sufficient. A more nuanced algorithm (such as the framework developed in this study) is certainly needed to better characterize the diurnal variation of ET.

In summary, the main advantages of our developed framework (compared to the conventionally used linear scaling approach) are twofold. First, it can account for the influence of other factors (e.g., environmental stress and biome types) other than incoming radiation; for example, it can produce certain degree of diurnal hysteresis due to high VPD and stomatal closure in the afternoon, while the ET scaled with  $SW_{in}$  (often symmetrical on clear days) is unable to do so. Second, with continuous LST constructed in the first step, our framework can generate continuous ET time series on days when native ECOSTRESS data are not available. In contrast, the linear scaling with  $SW_{in}$  can only provide diurnally resolved ET for days when there is ECOSTRESS overpass, therefore is unable to generate a continuous time series of diurnally resolved ET.

### 5.3. The Performance of DTC Under Cloudy Conditions

In the test domain centered at US-Seg, the first two time windows showed slightly degraded performance compared to the third one (Figures 6 and 8), partly due to the occurrence of cloud and rain events (Figure S1 in Supporting Information S1, note that rainy days were excluded from our statistical evaluation). During cloudy and rainy periods, both ECOSTRESS and GOES LST observations are less available, affecting the goodness of fit for the DTC model. Moreover, as the DTC model itself assumes and prescribes a diurnal LST shape under clear-sky conditions only, the LST construction could lead to “clear-sky bias” when the actual LST variation deviates from the prescribed shape due to the presence of clouds (e.g., 6 and 12 August 2018 and 12 April 2020 in Figure 7).

Currently, there are generally three broad types of approaches that are often applied to fill cloud-induced temporal gaps in thermal remote sensing-based LST (Martins et al., 2019). The first type of approach employs statistical interpolation to construct LST using clear-sky data at neighboring pixels or on proximal dates (e.g., Crosson et al., 2012). The limitation of such approaches is that they usually provide LST estimates that would appear under clear-sky conditions instead of cloudy conditions (which therefore similarly results in “clear-sky bias”). In addition, such approaches may not be feasible when clouds affect a large area or a long period. The second type of approach utilizes LST data sets either derived from reanalysis (Desai et al., 2021; Shiff et al., 2021) or retrieved from microwave bands that can penetrate clouds (Duan et al., 2017; Dowling et al., 2021). However, reanalysis data sets can be biased by the model parameterization uncertainties (from both model structure and parameter deficiencies); microwave based LST can also contain bias compared to thermal infrared based estimates due to the discrepancies in their retrieval algorithms (Ermida et al., 2017). In addition, these data sets are generally at very coarse spatial resolutions ( $>10$  km), which cannot resolve fine spatial details especially in heterogeneous landscapes. All these factors make it challenging to apply them in our case to fill the gap of LST at the 70 m resolution. The third type of approach employs a surface energy balance model to estimate LST under cloud cover (e.g., Jin & Dickinson, 2000; Lu et al., 2011). These approaches can also suffer from uncertainties in model parameterizations. To apply it to our case, meteorological measurements at high spatial and temporal resolutions are required, which are not readily available. Therefore, it is still very challenging to effectively and accurately estimate LST under cloudy conditions for our case (i.e., at very high spatial resolution) with existing approaches, which certainly deserves more research in the future.

### 5.4. Local Bias in ET Calculated From the PT-JPL Model

In our test in both domains, the constructed ET matched well with the native ECOSTRESS ET (if the same meteorological and reflectance data sets were used). However, they might present a bias when compared to in situ flux tower measurements. We chose to apply the PT-JPL ET model in this study because it is one of the default algorithms used to derive the official operational ECOSTRESS ET product. ECOSTRESS ET showed overall good agreement with flux tower ET when measurements from all selected sites and time periods were pooled together for analyses (Fisher et al., 2020), suggesting the overall effectiveness of the PT-JPL model in estimating subdaily

ET. In addition, the PT-JPL model has shown its capability in characterizing the spatial and temporal variation of ET over large geographical regions and seasonal scales (and beyond) (Chen et al., 2014; Ershadi et al., 2014; Fisher et al., 2008; McCabe et al., 2016; Michel et al., 2016; Miralles et al., 2016; Vinukollu et al., 2011).

However, the PT-JPL model can still lead to bias due to model parameterization uncertainties, as every model of the similar sort does (Jiménez et al., 2011; Long et al., 2014; Mueller et al., 2011). This is especially the case when the PT-JPL model is examined at small spatial scales (in particular, with heterogeneous landscapes) and/or short time scales (e.g., a 10-day time window), as shown in this study. For example, the ECOSTRESS ET uncertainty, defined as the standard deviation of instantaneous ET calculated with the PT-JPL model and two other physics-based models (Mu et al., 2007, 2011; Su, 2002) using the same input data sets, is at a similar magnitude of ECOSTRESS ET itself for shrublands and grasslands in the domain centered at US-Seg (Figure S9 in Supporting Information S1).

As this study makes the first effort, to the best of our knowledge, to directly resolve the diurnal cycle of ECOSTRESS ET, it is legitimate to start from the official PT-JPL algorithm. However, we acknowledge its uncertainties and here attempt to identify potential solutions that the ECOSTRESS team may focus on to improve the operational products in the future. It is promising that, as shown in this study, with slightly calibrating the equation for the soil moisture constraint, the modeled ET can reasonably match the magnitude of the in situ ET. Remote sensing ET modeling is still an ongoing and active research field and is being continuously improved. In fact, our results have led to an update in the next collection of ECOSTRESS ET that will incorporate soil moisture (Purdy et al., 2018). The improved PT-JPL model can be readily implemented in our framework to improve the accuracy of ET estimation in the future. Also note that with remote sensing LST as a major input for ET models, our derived diurnal LST in this study is readily applied to other ET models toward deriving diurnal ET products.

### 5.5. Availability of the Input Data Sets

The nominal revisit cycle of ECOSTRESS is 1–5 days. With agreement achieved between leave-one-out estimations and withheld observations in our tests (Figures 6 and 15a), we have demonstrated that our framework can reliably construct diurnal LST when the gap is approximately a week long provided that GOES LST is generally available. However, there might be longer periods, especially in regions and periods that are cloudy, when ECOSTRESS and GOES measurements may not be available. Interruption of data acquisition due to instrumental issues (e.g., the ECOSTRESS data acquisition gap from 29 September to 5 December in 2018 as a result of anomaly in the primary mass storage unit) may impede the LST diurnal cycle construction as well. Cross instrument calibration and data fusion of LST measurements from different platforms, for example, MODIS, Landsat 8, ECOSTRESS, and GOES could enrich the data availability and potentially alleviate the data gap issue (e.g., Anderson et al., 2021; Desai et al., 2021). In terms of ET, its calculation also depends on the availability of ancillary data sets, such as the Landsat 8 surface reflectance, which has a revisit cycle of 16 days and may lead to data bias during temporal interpolation. For the domain centered at US-ARM in this study, we tested the feasibility of employing the HLS data set when Landsat 8 reflectance data were less available due to clouds. The HLS data set effectively filled the data gaps of Landsat-8 and led to plausible ET estimation. The next ECOSTRESS data release will also incorporate Sentinel-2 and deliver the day-of-overpass NDVI and albedo for each ECOSTRESS acquisition.

### 5.6. Quality of the Input Data Sets

With multiple data sets as input (e.g., ECOSTRESS, GOES, MERRA-2, Landsat 8, and HLS), their respective biases and/or uncertainties could propagate into the final diurnally resolved LST and/or ET products. For example, ECOSTRESS LST has uncertainty about 1°C (Hulley et al., 2021, Figure S8 in Supporting Information S1), in a similar magnitude of RMSE in our leave-one-out validation (Figure 5e). In the test at US-ARM, we found that the positive bias of ECOSTRESS LST (relative to the in situ LST) might lead to an overestimation of the constructed LST (Figure 16a). ECOSTRESS LST also experiences reduced spatial resolution with larger viewing angles (e.g., >20°) at the edge of the swaths, as illustrated in Anderson et al. (2021). MERRA-2, although showed general agreement with tower meteorological measurements, bias was still observed during specific periods (e.g., with occurrence of rain events or local clouds, Figures S2 and S3 in Supporting Information S1), which could further propagate to the derived ET (Figure 11). This is consistent with previous findings that discrepancy in

forcing data can lead to differences in the calculated ET (e.g., Badgley et al., 2015; Gomis-Cebolla et al., 2019). In addition, MERRA-2 meteorological data sets are at a fairly coarse resolution (longitude  $0.625^\circ \times$  latitude  $0.5^\circ$ ). The inclusion of finer resolution meteorological data sets (e.g., from GEOS-FP) in the future ECOSTRESS release may better characterize the subgrid spatial variability and further improve the ET estimation. Indeed, our sensitivity test indicated that some of the diurnal fluctuations in tower ET could be well captured if more realistic meteorological measurements are employed as input to the PT-JPL model (Figure 11).

### 5.7. Other Possible Approaches to Construct Diurnal ECOSTRESS LST and ET

To construct diurnal ET, we took a strategy of constructing diurnal LST first as an intermediate step. This is because, compared to ET that is highly dynamic during the diurnal course, LST is a variable with relatively regular diurnal shapes that can be effectively fitted with a prescribed curve. Then we utilized the PT-JPL model to estimate diurnal ET from diurnal LST. With both steps mainly physically based, an alternative approach is using statistical or machine learning (ML) algorithms, such as employed by Jung et al. (2009, 2011) and Bodesheim et al. (2018). While our framework can run efficiently for a local region and specific time window, ML models usually require much more data for model training and can be computationally expensive. More importantly, sampling bias of different times of day, different seasons (due to data gaps), and different land cover types needs to be carefully considered if using ML models. Pixelwise linear scaling could be a parsimonious and practical approach (Chang et al., 2022; Desai et al., 2021). For example, Desai et al. (2021) fit a simple linear regression between fine resolution ECOSTRESS and coarse resolution GOES to construct diurnal LST at the fine spatial resolution. The caveat of such an approach is that it assumes the regression coefficients are universal across the whole time period, regardless of the time of a day, seasons, and disturbances, which may not be the case in reality. Therefore, there might be biases if the scaling coefficients vary with time, for example, different growing stages of crops, which in principle could be effectively accounted for by our approach using local windows. Nevertheless, all the approaches discussed here hold promise in resolving the target problem, that is, constructing the full diurnal cycle of ECOSTRESS LST and ET. Cross comparison of these approaches is certainly worth exploration in the future.

### 5.8. Potential Applications Enabled With the Diurnally Resolved LST and ET at High Spatial Resolution

As a pilot study, this study sets the stage for applying, testing, and further refining the framework developed here in regions with different climatic conditions and biome types. The ultimate goal is producing high resolution (70 m) diurnally resolved global LST and ET products. Such products will substantially facilitate numerous applications in ecology, hydrology, and agriculture.

In the test for the domain centered at US-Seg, our constructed LST showed that although all the land cover types exhibited similar diurnal shapes (i.e., reached daily LST maximum shortly after noon and presented diurnal asymmetry and hysteresis), there were still large differences in the diurnal variations among different land covers (Figure 20a). For example, shrublands/grasslands showed faster LST increase in the morning and a greater peak LST, compared to other vegetation types. Urban areas, with buildings and pavements, also absorbed heat quickly in the morning and presented high LST in the midday. Wetlands and croplands, with more water availability (e.g., from the nearby river or irrigation), showed much lower LST during the daytime, as a great portion of heat could be dissipated through evaporation and transpiration. Forests also showed comparatively lower LST in the daytime as a result of the evaporative cooling effect but presented a slightly higher LST in the early morning, possibly because the dense canopies could reduce heat loss from radiation and convection at nighttime. Compared to LST, the constructed ET presented a more symmetrical diurnal pattern, largely driven by the net radiation (Figure 20b). Wetlands and croplands presented the highest daytime ET, followed by forests, while urban areas and shrublands/grasslands showed much lower daytime ET. These results suggest that the constructed LST and ET can offer valuable information about the diurnal dynamics as well as provide guidance for water management for agricultural lands and ecological zones at much augmented spatial and temporal resolutions that are previously unavailable (Xiao et al., 2021).

Recently, Li et al. (2021) demonstrated that instantaneous gross primary production (GPP) can be estimated with ECOSTRESS instantaneous LST using a machine learning model. The constructed diurnally resolved LST developed in this study can be readily used as input to derive diurnal GPP, therefore provide key information about the diurnal cycle of vegetation growth and carbon uptake at high spatial resolution (70 m).

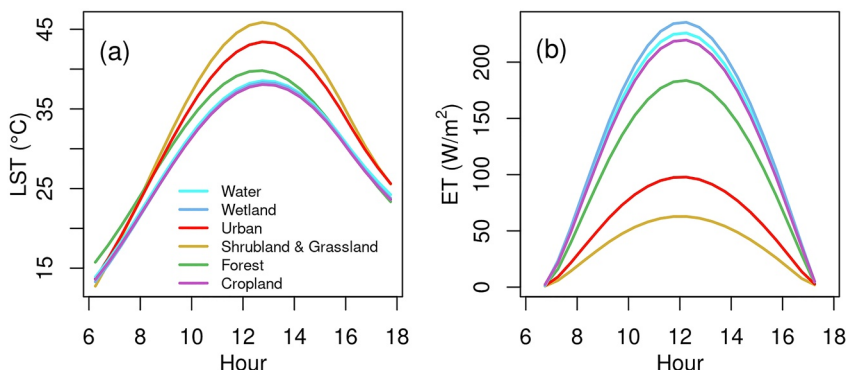


**Figure 20.** Diurnal variation of the constructed (a) Land surface temperature (LST) and (b) Evapotranspiration (ET) for different land cover types in the  $0.3^\circ \times 0.3^\circ$  domain centered at US-Seg on 27 September 2020. The full hourly time series of LST and ET mapping in this test domain during 26 September and 5 October 2020 is animated in Figure S10 in Supporting Information S1.

Finally, as LST is an important variable that regulates the biophysical processes of the ecosystems, and ET and GPP provide direct quantification of water and carbon exchange between ecosystems and atmosphere, the constructed data sets can therefore provide vital information about the ecosystems and help to improve benchmarking Earth system models at a much higher spatial and temporal resolutions than previously possible.

## 6. Conclusion

The ECOSTRESS mission provides LST and ET at high spatial resolution with sporadic diurnal samplings. To fully realize the potential of ECOSTRESS and take advantage of its diurnal acquisition characteristics, we developed a framework to construct the clear-sky continuous diurnal cycle of ECOSTRESS LST and ET from the native sporadic measurements and tested it in a relatively homogeneous semiarid grassland landscape and a heterogeneous humid cropland landscape. The constructed LST and ET successfully reproduced the spatio-temporal pattern of native ECOSTRESS observations. In addition, the constructed LST and ET showed overall consistency (especially under clear-sky conditions) with independent in situ LST and ET from two sites, that is, US-Seg and US-ARM, across various phenological stages. As the first study of its kind, our analysis serves as an initial demonstration of the effectiveness of our framework and sets the stage for the ultimate goal of developing  $<100$  m diurnally resolved global LST and ET products. These products will substantially contribute to agricultural monitoring and decision-making as well as Earth system model benchmarking at much augmented spatial and temporal resolutions.

## Appendix A: Notations Used in the DTC Model

Table A1

**Table A1**  
*Notations Used in the DTC Model*

Symbols	Definition	Derivation
$t$	Time of day	
$t_{\text{sr},d}$	Sunrise of day $d$	Calculated based on dates and coordinates using R “suncalc” package ( <a href="https://cran.r-project.org/web/packages/suncalc/">https://cran.r-project.org/web/packages/suncalc/</a> ) and assumed to be constant during each 10-day time window in this study
$t_{\text{sr},d+1}$	Sunrise of day $d + 1$	same as $t_{\text{sr},d}$
$t_{\max}$	Time when LST reaches the daily maximum	Calibrated
$t_{\text{ss}}$	Actual sunset of day $d$	$t_{\text{ss}} = t_s + 1$

**Table A1**  
*Continued*

Symbols	Definition	Derivation
$t_s$	Thermal sunset when the nighttime attenuation starts	Calibrated
$LST(t)$	LST at time $t$	Equations 1a and 1b
$T_{sr,d}$	LST at sunrise of day $d$	Calibrated
$T_{sr,d+1}$	LST at sunrise of day $d + 1$	Calibrated
$T_{max,d}$	LST maximum of day $d$	Calibrated
$T_0$	Residual temperature around sunrise	$T_0 = T_{sr,d} + T_a \cos(\pi/4)$
$T_a$	Temperature amplitude	$T_a = \frac{T_{max,d} - T_{sr,d}}{\cos(\pi/4+1)}$
$\omega$	Width over the half period of the cosine term	$\omega = \frac{4}{3}t_{max}$
$\delta T$	Temperature difference between $T_0$ and $T(t \rightarrow \infty)$	$\delta T = \frac{T_a [\cos(u)(T_a \cos(u) + T_0 - T_{sr,d+1}) + (\pi/\omega) \sin(u)(24 - t_s)(T_0 - T_{sr,d+1})]}{T_0 - T_{sr,d+1} - T_a ((\pi/\omega) \sin(u)(24 - t_s) - \cos(u))}$
$k$	Attenuation constant	$k = \frac{T_a \cos(u) - \delta T}{T_a \pi \sin(u)}$
$u$	No physical meaning, used to simplify the expressions	$u = \frac{\pi}{\omega}(t_s - t_{max})$

Note. All the time-related terms, that is,  $t$ ,  $t_{max}$ ,  $t_s$ , and  $t_{ss}$ , are calculated as hours after sunrise of day  $d$ . All the temperature-related terms are in the unit of °C.

## Appendix B: Notations in the PT-JPL Model

Tables B1, B2, B3, B4, B5 and B6

**Table B1**  
*ET Variables ( $W m^{-2}$ )*

Symbols	Definition	Derivation
ET	Total evapotranspiration	$ET = ET_c + ET_s + ET_i$
$ET_c$	Transpiration from canopy	$ET_c = (1 - f_{wet}) f_g f_T f_M \alpha^{\frac{\Delta}{\Delta+\gamma}} R_{nc}$
$ET_s$	Evaporation from soil	$ET_s = (f_{wet} + f_{SM})(1 - f_{wet}) \alpha^{\frac{\Delta}{\Delta+\gamma}} (R_{ns} - G)$
$ET_i$	Evaporation from surface interception	$ET_i = f_{wet} \alpha^{\frac{\Delta}{\Delta+\gamma}} R_{nc}$

**Table B2**  
*ET Downregulation Constraint Factors (Unitless, Bounded to 0–1)*

Symbols	Definition	Derivation
$f_g$	Green canopy fraction	$f_g = f_{APAR}/f_{IPAR}$
$f_M$	Plant moisture constraint	$f_M = f_{APAR}/f_{APARmax}$
$f_{wet}$	Relative surface wetness	$f_{wet} = RH^4$
$f_{SM}$	Soil moisture constraint	$f_{SM} = RH^{VPD}$
$f_T$	Plant temperature constraint	$f_T = e^{-\left(\frac{T_{air}-T_{opt}}{T_{opt}}\right)^2}$

Note. Instantaneous RH is used to calculate  $f_{wet}$ , while 2-week forward average of RH, VPD, and  $T_{air}$  are used to calculate  $f_{SM}$  and  $f_T$ .

**Table B3**  
*Radiation Variables ( $W m^{-2}$ )*

Symbols	Definition	Derivation/Data source
$R_n$	Net radiation	$R_n = SW_{in} - SW_{out} + LW_{in} - LW_{out}$
$SW_{in}$	Downwelling shortwave radiation	MERRA-2
$SW_{out}$	Upwelling shortwave radiation	$SW_{out} = \text{albedo} \cdot SW_{in}$
$LW_{in}$	Downwelling longwave radiation	MERRA-2
$LW_{out}$	Upwelling longwave radiation	$LW_{out} = \sigma \cdot \epsilon \cdot LST^4$
$R_{ns}$	Net radiation to the soil	$R_{ns} = R_n e^{-0.6LAI}$
$R_{nc}$	Net radiation to the canopy	$R_{nc} = R_n - R_{ns}$
$G$	Ground heat flux	$G = R_n (0.05 + 0.265 (1 - f_{IPAR}))$

**Table B4**  
*Vegetation Property Variables (Unitless)*

Symbols	Definition	Derivation/Data source
NDVI	Normalized difference vegetation index	$NDVI = \frac{r_{NIR} - r_{red}}{r_{NIR} + r_{red}}$
$r_{NIR}$	Near infrared band reflectance	Landsat 8 or HLS
$r_{red}$	Red band reflectance	Landsat 8 or HLS
SAVI	Soil-adjusted vegetation index	$SAVI = 0.45NDVI + 0.132$
$f_{APAR}$	Fraction of PAR absorbed by green vegetation cover	$f_{APAR} = 1.928 NDVI - 0.274$ , revised from $f_{APAR} = 1.3632 SAVI - 0.048$ that was used in the default PT-JPL model, to better characterize the vegetation cover in the tested regions.
$f_{APARmax}$	$f_{APAR}$ annual maximum	$\max(f_{APAR})$
$f_{IPAR}$	Fraction of PAR intercepted by total vegetation cover	$f_{IPAR} = NDVI - 0.05$
LAI	Leaf area index	$LAI = -\ln(1 - f_{IPAR}) / 0.5$

**Table B5**  
*Meteorological Variables*

Symbols	Definition	Derivation/Data source
$\Delta$	Slope of the saturation-to-vapor pressure curve (kPa/ $^{\circ}\text{C}$ )	$\Delta = \frac{240.97 \times 17.502 e_a}{(T_a + 240.97)^2}$
$\gamma$	Psychrometric constant (kPa/ $^{\circ}\text{C}$ )	$\gamma = 0.066$
$T_{air}$	Near surface air temperature ( $^{\circ}\text{C}$ )	MERRA-2
$T_{dew}$	Dew point temperature ( $^{\circ}\text{C}$ )	MERRA-2
$e_a$	Water vapor pressure (kPa)	$e_a = 0.613753 e^{\frac{17.277 T_{dew}}{240.97 + T_{dew}}}$
$e_s$	Saturation vapor pressure (kPa)	$e_s = 0.61121 e^{\frac{17.502 T_{air}}{240.97 + T_{air}}}$
VPD	Atmospheric vapor pressure deficit (kPa)	$VPD = e_s - e_a$
RH	Relative humidity	$RH = \frac{e_a}{e_s}$
$T_{opt}$	Optimal air temperature ( $^{\circ}\text{C}$ )	$T_{opt} = T_a \text{ at phenology} \left( R_n T_{air} \frac{SAVI}{VPD} \right) \text{maximum}$

Note.  $R_n$ ,  $T_{air}$ , SAVI, and VPD used to calculate  $T_{opt}$  are all 2-week forward averages.

**Table B6**

*Parameters*

Symbols	Definition	Values/Data source
$\alpha$	PT coefficient	$\alpha = 1.26$
$\sigma$	The Stefan-Boltzmann constant ( $\text{W m}^{-2} \text{K}^{-4}$ )	$\sigma = 5.67 \times 10^{-8}$
$\epsilon$	Surface emissivity	ECOSTRESS
Albedo	Shortwave albedo	$\text{albedo} = 0.356r_{\text{blue}} + 0.130r_{\text{red}} + 0.373r_{\text{NIR}} + 0.085r_{\text{SWIR1}} + 0.072r_{\text{SWIR2}} - 0.0018$

Note.  $r_{\text{blue}}$ ,  $r_{\text{red}}$ ,  $r_{\text{NIR}}$ ,  $r_{\text{SWIR1}}$ , and  $r_{\text{SWIR2}}$  are band reflectances from Landsat 8 or HLS.

## Data Availability Statement

All the data sets used in this study are publicly available: ECOSTRESS data can be accessed through <https://lpdaacs.crs.usgs.gov/appears/>; GOES LST can be assessed from <https://www.avl.class.noaa.gov/>; MERRA-2 data can be accessed from <https://disc.gsfc.nasa.gov/>. Landsat 8 data can be accessed through google earth engine [https://developers.google.com/earth-engine/datasets/catalog/LANDSAT\\_LC08\\_C01\\_T1\\_SR](https://developers.google.com/earth-engine/datasets/catalog/LANDSAT_LC08_C01_T1_SR); HLS v2 data can be accessed from <https://lpdac.usgs.gov>; US-Seg flux tower data can be downloaded from <https://ameriflux.lbl.gov>; and Land cover data can be downloaded from <https://nassgeodata.gmu.edu/CropScape>.

## Acknowledgments

This project is supported by National Aeronautics and Space Administration (NASA) Jet Propulsion Laboratory (JPL) Strategic University Research Partnership (SURP) award 1641697. JW and YS also acknowledge support from NASA CMS (80NSSC21K1058). JW also acknowledges support from NASA FINESST fellowship 80NSSC20K1646. JBF and NCP carried out the research at the JPL, California Institute of Technology, under a contract with NASA (80NNM0018D0004) and funded through the SURP program. JBF was supported by ECOSTRESS. LH is partly supported by NASA IDS (80NSSC20K1263) and HAQAST (80NSSC21K0430) programs. US-Seg flux tower operation, data processing is supported by grants to MEL from Department of Energy AmeriFlux Management Project (subcontract no. 7074628) and NSF Sevilleta LTER (NSF-DEB LTER 1440478).

## References

- Allen, R. G., Pereira, L. S., Raes, D., & Smith, M. (1998). *Crop evapotranspiration: Guidelines for computing crop water requirements (FAO Irrigation and Drainage Paper)* (p. 328). FAO - Food and Agriculture Organization of the United Nations.
- Allen, R. G., Tasumi, M., Morse, A., & Trezza, R. (2005). A Landsat-based energy balance and evapotranspiration model in Western US water rights regulation and planning. *Irrigation and Drainage Systems*, 19(3), 251–268. <https://doi.org/10.1007/S10795-005-5187-Z>
- Anderson, M. C., Allen, R. G., Morse, A., & Kustas, W. P. (2012). Use of Landsat thermal imagery in monitoring evapotranspiration and managing water resources. <https://doi.org/10.1016/j.rse.2011.08.025>
- Anderson, M. C., Kustas, W. P., Norman, J. M., Hain, C. R., Mecikalski, J. R., Schultz, L., et al. (2011). Hydrology and Earth System Sciences mapping daily evapotranspiration at field to continental scales using geostationary and polar orbiting satellite imagery. *Hydrology and Earth System Sciences*, 15(1), 223–239. <https://doi.org/10.5194/hess-15-223-2011>
- Anderson, M. C., Norman, J. M., Diak, G. R., Kustas, W. P., & Mecikalski, J. R. (1997). A two-source time-integrated model for estimating surface fluxes using thermal infrared remote sensing. *Remote Sensing of Environment*, 60(2), 195–216. [https://doi.org/10.1016/S0034-4257\(96\)00215-5](https://doi.org/10.1016/S0034-4257(96)00215-5)
- Anderson, M. C., Yang, Y., Xue, J., Knipper, K. R., Yang, Y., Gao, F., et al. (2021). Interoperability of ECOSTRESS and Landsat for mapping evapotranspiration time series at sub-field scales. *Remote Sensing of Environment*, 252, 112189. <https://doi.org/10.1016/j.rse.2020.112189>
- Anderson-Teixeira, K. J., Delong, J. P., Fox, A. M., Brese, D. A., & Litvak, M. E. (2011). Differential responses of production and respiration to temperature and moisture drive the carbon balance across a climatic gradient in New Mexico. *Global Change Biology*, 17(1), 410–424. <https://doi.org/10.1111/j.1365-2486.2010.02269.x>
- AppEEARS Team. (2020). *Application for Extracting and Exploring Analysis Ready Samples (AppEEARS)*. Ver. X.X. NASA EOSDIS Land Processes Distributed Active Archive Center (LPDAAC), USGS/Earth Resources Observation and Science (EROS) Center. Retrieved from <https://lpdaacs.crs.usgs.gov/appears/>
- Badgley, G., Fisher, J. B., Jiménez, C., Tu, K. P., & Vinukollu, R. (2015). On uncertainty in global terrestrial evapotranspiration estimates from choice of input forcing datasets. *Journal of Hydrometeorology*, 16(4), 1449–1455. <https://doi.org/10.1175/JHM-D-14-0040.1>
- Baldocchi, D. (2014). Measuring fluxes of trace gases and energy between ecosystems and the atmosphere - The state and future of the eddy covariance method. *Global Change Biology*, 20(12), 3600–3609. <https://doi.org/10.1111/gcb.12649>
- Baldocchi, D. D., Hincks, B. B., & Meyers, T. P. (1988). Measuring biosphere-atmosphere exchanges of biologically related gases with micrometeorological methods. *Ecology*, 69(5), 1331–1340. <https://doi.org/10.2307/1941631>
- Biraud, S., Fischer, M., Chan, S., & Torn, M. (2021). AmeriFlux BASE US-ARM ARM Southern Great Plains site- Lamont, Ver. 11-5 [Dataset]. AmeriFlux AMP. <https://ameriflux.lbl.gov/doi/AmeriFlux/US-ARM/>
- Bodesheim, P., Jung, M., Gans, F., Mahecha, M. D., & Reichstein, M. (2018). Upscaled diurnal cycles of land-atmosphere fluxes: A new global half-hourly data product. *Earth System Science Data*, 10(3), 1327–1365. <https://doi.org/10.5194/essd-10-1327-2018>
- Bonan, G. B. (2008). Forests and climate change: Forcings, feedbacks, and the climate benefits of forests. *Science*, 320(5882), 1444–1449. <https://doi.org/10.1126/science.1155121>
- Bouchet, R. J. (1963). Evapotranspiration réelle, evapotranspiration potentielle, et production agricole. *Annales Agronomiques*, 14, 743–824.
- Bowen, I. S. (1926). The ratio of heat losses by conduction and by evaporation from any water surface. *Physics Reviews*, 27(6), 779–787. <https://doi.org/10.1103/PhysRev.27.779>
- Brutsaert, W. (2015). A generalized complementary principle with physical constraints for land-surface evaporation. *Water Resources Research*, 51(10), 8087–8093. <https://doi.org/10.1002/2015WR017720>
- Brutsaert, W., Cheng, L., & Zhang, L. (2020). Spatial distribution of global landscape evaporation in the early twenty-first century by means of a generalized complementary approach. *Journal of Hydrometeorology*, 21(2), 287–298. <https://doi.org/10.1175/JHM-D-19-0208.1>
- Cammalleri, C., Anderson, M. C., & Kustas, W. P. (2014). Upscaling of evapotranspiration fluxes from instantaneous to daytime scales for thermal remote sensing applications. *Hydrology and Earth System Sciences*, 18(5), 1885–1894. <https://doi.org/10.5194/hess-18-1885-2014>

- Cawse-Nicholson, K., Braverman, A., Kang, E. L., Li, M., Johnson, M., Halverson, G., et al. (2020). Sensitivity and uncertainty quantification for the ECOSTRESS evapotranspiration algorithm – DisALEXI. *International Journal of Applied Earth Observation and Geoinformation*, 89, 102088. <https://doi.org/10.1016/j.jag.2020.102088>
- Chang, Y., Xiao, J., Li, X., Zhou, D., & Wu, Y. (2022). Combining GOES-R and ECOSTRESS land surface temperature data to investigate diurnal variations of surface urban heat island. *Science of The Total Environment*, 823, 153652. <https://doi.org/10.1016/j.scitotenv.2022.153652>
- Chen, Y., Xia, J., Liang, S., Feng, J., Fisher, J. B., Li, X., et al. (2014). Comparison of satellite-based evapotranspiration models over terrestrial ecosystems in China. *Remote Sensing of Environment*, 140, 279–293. <https://doi.org/10.1016/j.rse.2013.08.045>
- Cook, D. R. (2007). *Energy Balance Bowen Ratio (EBBR) handbook*, Climate Research Facility. U.S. Department of Energy. Retrieved from <http://www.arm.gov/instruments/ebsr>
- Crosson, W. L., Al-Hamdan, M. Z., Hemmings, S. N. J., & Wade, G. M. (2012). A daily merged MODIS Aqua-Terra land surface temperature data set for the conterminous United States. *Remote Sensing of Environment*, 119, 315–324. <https://doi.org/10.1016/j.rse.2011.12.019>
- Desai, A. R., Khan, A. M., Zheng, T., Paleri, S., Butterworth, B., Lee, T. R., et al. (2021). Multi-sensor approach for high space and time resolution land surface temperature. *Earth and Space Science*, 8(10), e2021EA001842. <https://doi.org/10.1029/2021EA001842>
- Dhungel, R., Aiken, R., Evett, S. R., Colaizzi, P. D., Marek, G., Moorhead, J. E., et al. (2021). Energy imbalance and evapotranspiration hysteresis under an advective environment: Evidence from lysimeter, eddy covariance, and energy balance modeling. *Geophysical Research Letters*, 48(1), 1–12. <https://doi.org/10.1029/2020GL091203>
- Dowling, T. P. F., Song, P., Jong, M. C., Merbold, L., Wooster, M. J., Huang, J., & Zhang, Y. (2021). An improved cloud gap-filling method for longwave infrared land surface temperatures through introducing passive microwave techniques. *Remote Sensing*, 13(17), 1–26. <https://doi.org/10.3390/rs13173522>
- Duan, S. B., Li, Z. L., & Leng, P. (2017). A framework for the retrieval of all-weather land surface temperature at a high spatial resolution from polar-orbiting thermal infrared and passive microwave data. *Remote Sensing of Environment*, 195, 107–117. <https://doi.org/10.1016/j.rse.2017.04.008>
- Duan, S.-B., Li, Z.-L., Tang, B.-H., Wu, H., Tang, R., Bi, Y., & Zhou, G. (2014). Estimation of diurnal cycle of land surface temperature at high temporal and spatial resolution from clear-sky MODIS data. *Remote Sensing*, 6(4), 3247–3262. <https://doi.org/10.3390/rs6043247>
- Duman, T., Huang, C.-W., & Litvak, M. E. (2021). Recent land cover changes in the Southwestern US lead to an increase in surface temperature. *Agricultural and Forest Meteorology*, 297(May 2020), 108246. <https://doi.org/10.1016/j.agrformet.2020.108246>
- Ermida, S. L., Jiménez, C., Prigent, C., Trigo, I. F., & DaCamara, C. C. (2017). Inversion of AMSR-E observations for land surface temperature estimation: 2. Global comparison with infrared satellite temperature. *Journal of Geophysical Research: Atmospheres*, 122(6), 3348–3360. <https://doi.org/10.1002/2016JD026148>
- Ershadi, A., McCabe, M. F., Evans, J. P., Chaney, N. W., & Wood, E. F. (2014). Multi-site evaluation of terrestrial evaporation models using FLUXNET data. *Agricultural and Forest Meteorology*, 187, 46–61. <https://doi.org/10.1016/j.agrformet.2013.11.008>
- Falge, E., Aubinet, M., Bakwin, P. S., Baldocchi, D., Berbigier, P., Bernhofer, C., et al. (2017). *FLUXNET research network site characteristics, investigators, and bibliography*, 2016. ORNL DAAC. <https://doi.org/10.3334/ORNLDAAC/1530>
- Fang, L., Zhan, X., Schull, M., Kalluri, S., Laszlo, I., Yu, P., et al. (2019). Evapotranspiration data product from NESDIS GET-D system upgraded for GOES-16 ABI observations. *Remote Sensing*, 11(22), 2639. <https://doi.org/10.3390/rs11222639>
- Fischer, M. L., Billesbach, D. P., Berry, J. A., Riley, W. J., & Torn, M. S. (2007). Spatiotemporal variations in growing season exchanges of CO<sub>2</sub>, H<sub>2</sub>O, and sensible heat in agricultural fields of the Southern Great Plains. *Earth Interactions*, 11(17), 1–21. <https://doi.org/10.1175/EI231.1>
- Fisher, J. B., & ECOSTRESS algorithm development team. (2015). *ECOSystem Spaceborne Thermal Radiometer Experiment on Space Station (ECOSTRESS): Level-3 evapotranspiration LE (ET\_PT-JPL) algorithm theoretical basis document (ATBD)*. Rep., (p. 24). Jet Propulsion Laboratory.
- Fisher, J. B., Lee, B., Purdy, A. J., Halverson, G. H., Dohlen, M. B., Cawse-Nicholson, K., et al. (2020). ECOSTRESS: NASA's next generation mission to measure evapotranspiration from the International Space Station. *Water Resources Research*, 56(4), 1–20. <https://doi.org/10.1029/2019WR026058>
- Fisher, J. B., Melton, F., Middleton, E., Hain, C., Anderson, M., Allen, R., et al. (2017). The future of evapotranspiration: Global requirements for ecosystem functioning, carbon and climate feedbacks, agricultural management, and water resources. *Water Resources Research*, 53(4), 2618–2626. <https://doi.org/10.1002/2016WR020175>
- Fisher, J. B., Tu, K. P., & Baldocchi, D. D. (2008). Global estimates of the land-atmosphere water flux based on monthly AVHRR and ISLSCP-II data, validated at 16 FLUXNET sites. *Remote Sensing of Environment*, 112(3), 901–919. <https://doi.org/10.1016/j.rse.2007.06.025>
- Gillespie, A., Rokugawa, S., Matsunaga, T., Steven Cothern, J., Hook, S., & Kahle, A. B. (1998). A temperature and emissivity separation algorithm for advanced spaceborne thermal emission and reflection radiometer (ASTER) images. *IEEE Transactions on Geoscience and Remote Sensing*, 36(4), 1113–1126. <https://doi.org/10.1109/36.700995>
- Global Modeling and Assimilation Office (GMAO). (2015a). *MERRA-2 tavg1\_2d\_rad\_Nx: 2d,1-hourly, time-averaged, single-level, assimilation, radiation diagnostics V5.12.4*. Goddard Earth Sciences Data and Information Services Center (GES DISC). <https://doi.org/10.5067/Q9QMY5PBNVIT>
- Global Modeling and Assimilation Office (GMAO). (2015b). *MERRA-2 tavg1\_2d\_slv\_Nx: 2d,1-hourly, time-averaged, single-level, assimilation, single-level diagnostics V5.12.4*. Goddard Earth Sciences Data and Information Services Center (GES DISC). <https://doi.org/10.5067/VJAFLII1CSIV>
- Gomis-Cebolla, J., Jimenez, J. C., Sobrino, J. A., Corbari, C., & Mancini, M. (2019). Intercomparison of remote-sensing based evapotranspiration algorithms over amazonian forests. *International Journal of Applied Earth Observation and Geoinformation*, 80, 280–294. <https://doi.org/10.1016/j.jag.2019.04.009>
- Goss, M. J., & Ehlers, W. (2009). The role of lysimeters in the development of our understanding of soil water and nutrient dynamics in ecosystems. *Soil Use and Management*, 25(3), 213–223. <https://doi.org/10.1111/j.1475-2743.2009.00230.X>
- Göttsche, F. M., & Olesen, F. S. (2001). Modelling of diurnal cycles of brightness temperature extracted from Meteosat data. *Remote Sensing of Environment*, 76(3), 337–348. [https://doi.org/10.1016/S0034-4257\(00\)00214-5](https://doi.org/10.1016/S0034-4257(00)00214-5)
- Halverson, G. (2018). *Near real-time monitoring of global evapotranspiration and its application to water resource management*. California State University.
- Hastie, T., Tibshirani, R., & Friedman, J. H. (2009). *The elements of statistical learning: Data mining, inference, and prediction* (2nd ed.). Springer.
- Hu, L., Sun, Y., Collins, G., & Fu, P. (2020). Improved estimates of monthly land surface temperature from MODIS using a diurnal temperature cycle (DTC) model. *ISPRS Journal of Photogrammetry and Remote Sensing*, 168, 131–140. <https://doi.org/10.1016/j.isprsjprs.2020.08.007>

- Hulley, G. C., Gottsche, F. M., Rivera, G., Hook, S. J., Freepartner, R. J., Martin, M. A., et al. (2021). Validation and quality assessment of the ECOSTRESS level-2 land surface temperature and emissivity product. *IEEE Transactions on Geoscience and Remote Sensing*, 60, 1–23. <https://doi.org/10.1109/TGRS.2021.3079879>
- Hulley, G. C., & Hook, S. J. (2011). Generating consistent land surface temperature and emissivity products between ASTER and MODIS data for Earth science research. *IEEE Transactions on Geoscience and Remote Sensing*, 49(4), 1304–1315. <https://doi.org/10.1109/TGRS.2010.2063034>
- Iwabuchi, H. (2006). Efficient Monte Carlo methods for radiative transfer modeling. *Journal of the Atmospheric Sciences*, 63(9), 2324–2339. <https://doi.org/10.1175/JAS3755.1>
- Jiang, C., & Ryu, Y. (2016). Multi-scale evaluation of global gross primary productivity and evapotranspiration products derived from Breathing Earth System Simulator (BESS). *Remote Sensing of Environment*, 186, 528–547. <https://doi.org/10.1016/j.rse.2016.08.030>
- Jiménez, C., Prigent, C., Mueller, B., Seneviratne, S. I., McCabe, M. F., Wood, E. F., et al. (2011). Global intercomparison of 12 land surface heat flux estimates. *Journal of Geophysical Research*, 116(2), D02102. <https://doi.org/10.1029/2010JD014545>
- Jin, M., & Dickinson, R. E. (2000). A generalized algorithm for retrieving cloudy sky skin temperature from satellite thermal infrared radiances. *Journal of Geophysical Research*, 105(D22), 27037–27047. <https://doi.org/10.1029/2000JD900318>
- Jung, M., Koitala, S., Weber, U., Ichii, K., Gans, F., Camps-Valls, G., et al. (2019). The FLUXCOM ensemble of global land-atmosphere energy fluxes. *Scientific Data*, 6(1), 1–14. <https://doi.org/10.1038/s41597-019-0076-8>
- Jung, M., Reichstein, M., & Bondeau, A. (2009). Towards global empirical upscaling of FLUXNET eddy covariance observations: Validation of a model tree ensemble approach using a biosphere model. *Biogeosciences*, 6(10), 2001–2013. <https://doi.org/10.5194/bg-6-2001-2009>
- Jung, M., Reichstein, M., Margolis, H. A., Cescatti, A., Richardson, A. D., Arain, M. A., et al. (2011). Global patterns of land-atmosphere fluxes of carbon dioxide, latent heat, and sensible heat derived from eddy covariance, satellite, and meteorological observations. *Journal of Geophysical Research*, 116(3), G00J07. <https://doi.org/10.1029/2010JG001566>
- Li, X., Xiao, J., Fisher, J. B., & Baldocchi, D. D. (2021). ECOSTRESS estimates gross primary production with fine spatial resolution for different times of day from the International Space Station. *Remote Sensing of Environment*, 258(March), 112360. <https://doi.org/10.1016/j.rse.2021.112360>
- Liang, S. (2001). Narrowband to broadband conversions of land surface albedo I. *Remote Sensing of Environment*, 76(2), 213–238. [https://doi.org/10.1016/S0034-4257\(00\)00205-4](https://doi.org/10.1016/S0034-4257(00)00205-4)
- Litvak, M. (2021). AmeriFlux BASE US-Seg Sevilleta grassland, Ver. 16-5. [Dataset]. AmeriFlux AMP. <https://doi.org/10.17190/AMF/1246124>
- Long, D., Longuevergne, L., & Scanlon, B. R. (2014). Uncertainty in evapotranspiration from land surface modeling, remote sensing, and GRACE satellites. *Water Resources Research*, 50(2), 1131–1151. <https://doi.org/10.1002/2013WR014581>
- Lu, L., Venus, V., Skidmore, A., Wang, T., & Luo, G. (2011). Estimating land-surface temperature under clouds using MSG/SEVIRI observations. *International Journal of Applied Earth Observation and Geoinformation*, 13(2), 265–276. <https://doi.org/10.1016/j.jag.2010.12.007>
- Ma, N., Szilagyi, J., Zhang, Y., & Liu, W. (2019). Complementary-relationship-based modeling of terrestrial evapotranspiration across China during 1982–2012: Validations and spatiotemporal analyses. *Journal of Geophysical Research: Atmospheres*, 124(8), 4326–4351. <https://doi.org/10.1029/2018JD029850>
- Martins, J. P. A., Trigo, I. F., Ghilain, N., Jimenez, C., Gottsche, F. M., Ermida, S. L., et al. (2019). An all-weather land surface temperature product based on MSG/SEVIRI observations. *Remote Sensing*, 11(24), 3044. <https://doi.org/10.3390/rs11243044>
- Masek, J., Ju, J., Roger, J., Skakun, S., Vermote, E., Claverie, M., et al. (2021a). HLS operational land imager surface reflectance and TOA brightness daily global 30m v2.0 [Dataset]. NASA EOSDIS Land Processes DAAC. <https://doi.org/10.5067/HLS/HLSL30.002>
- Masek, J., Ju, J., Roger, J., Skakun, S., Vermote, E., Claverie, M., et al. (2021b). HLS Sentinel-2 multi-spectral instrument surface reflectance daily global 30m v2.0 [Dataset]. NASA EOSDIS Land Processes DAAC. <https://doi.org/10.5067/HLS/HLSS30.002>
- Mccabe, M. F., Ershadi, A., Jimenez, C., Miralles, D. G., Michel, D., & Wood, E. F. (2016). The GEWEX LandFlux project: Evaluation of model evaporation using tower-based and globally gridded forcing data. *Geoscientific Model Development*, 9(1), 283–305. <https://doi.org/10.5194/gmd-9-283-2016>
- Menzel, W. P., & Purdom, J. F. W. (1994). Introducing GOES-I: The first of a new generation of geostationary operational environmental satellites. *Bulletin of the American Meteorological Society*, 75(5), 757–781. [https://doi.org/10.1175/1520-0477\(1994\)075<0757:igitfo>2.0.co;2](https://doi.org/10.1175/1520-0477(1994)075<0757:igitfo>2.0.co;2)
- Michel, D., Jiménez, C., Miralles, D. G., Jung, M., Hirschi, M., Ershadi, A., et al. (2016). The WACMOS-ET project-Part 1: Tower-scale evaluation of four remote-sensing-based evapotranspiration algorithms. *Hydrology and Earth System Sciences*, 20(2), 803–822. <https://doi.org/10.5194/hess-20-803-2016>
- Miralles, D. G., Holmes, T. R. H., De Jeu, R. A. M., Gash, J. H., Meesters, A. G. C. A., & Dolman, A. J. (2011). Hydrology and Earth System Sciences Global land-surface evaporation estimated from satellite-based observations. *Hydrology and Earth System Sciences*, 15(2), 453–469. <https://doi.org/10.5194/hess-15-453-2011>
- Miralles, D. G., Jiménez, C., Jung, M., Michel, D., Ershadi, A., Mccabe, M. F., et al. (2016). The WACMOS-ET project-Part 2: Evaluation of global terrestrial evaporation data sets. *Hydrology and Earth System Sciences*, 20(2), 823–842. <https://doi.org/10.5194/hess-20-823-2016>
- Monteith, J. L. (1965). Evaporation and environment. *Symposia of the Society for Experimental Biology*, 19, 205–224.
- Mu, Q., Heinsch, F. A., Zhao, M., & Running, S. W. (2007). Development of a global evapotranspiration algorithm based on MODIS and global meteorology data. *Remote Sensing of Environment*, 111(4), 519–536. <https://doi.org/10.1016/j.rse.2007.04.015>
- Mu, Q., Zhao, M., & Running, S. W. (2011). Improvements to a MODIS global terrestrial evapotranspiration algorithm. *Remote Sensing of Environment*, 115(8), 1781–1800. <https://doi.org/10.1016/j.rse.2011.02.019>
- Mueller, B., Seneviratne, S. I., Jimenez, C., Corti, T., Hirschi, M., Balsamo, G., et al. (2011). Evaluation of global observations-based evapotranspiration datasets and IPCC AR4 simulations. *Geophysical Research Letters*, 38(6). <https://doi.org/10.1029/2010GL046230>
- Nash, J. E., & Sutcliffe, J. V. (1970). River flow forecasting through conceptual models part I—a discussion of principles. *Journal of Hydrology*, 10(3), 282–290. [https://doi.org/10.1016/0022-1694\(70\)90255-6](https://doi.org/10.1016/0022-1694(70)90255-6)
- Nelson, J. A., Carvalhais, N., Migliavacca, M., Reichstein, M., & Jung, M. (2018). Water-stress-induced breakdown of carbon-water relations: Indicators from diurnal FLUXNET patterns. *Biogeosciences*, 15(8), 2433–2447. <https://doi.org/10.5194/bg-15-2433-2018>
- Priestley, C. H. B., & Taylor, R. J. (1972). On the assessment of surface heat flux and evaporation using large scale parameters. *Monthly Weather Review*, 100(2), 81–92. [https://doi.org/10.1175/1520-0493\(1972\)100<0081:otaosh>2.3.co;2](https://doi.org/10.1175/1520-0493(1972)100<0081:otaosh>2.3.co;2)
- Purdy, A. J., Fisher, J. B., Goulden, M. L., Colliander, A., Halverson, G., Tu, K., & Famiglietti, J. S. (2018). SMAP soil moisture improves global evapotranspiration. *Remote Sensing of Environment*, 219, 1–14. <https://doi.org/10.1016/j.rse.2018.09.023>
- Ramillien, G., Frappart, F., Güntner, A., Ngo-Duc, T., Cazenave, A., & Laval, K. (2006). Time variations of the regional evapotranspiration rate from Gravity Recovery and Climate Experiment (GRACE) satellite gravimetry. *Water Resources Research*, 42(10). <https://doi.org/10.1029/2005WR004331>

- Renner, M., Brenner, C., Mallick, K., Wizemann, H. D., Conte, L., Trebs, I., et al. (2019). Using phase lags to evaluate model biases in simulating the diurnal cycle of evapotranspiration: A case study in Luxembourg. *Hydrology and Earth System Sciences*, 23(1), 515–535. <https://doi.org/10.5194/hess-23-515-2019>
- Richardson, A. D., Hollinger, D. Y., Burba, G. G., Davis, K. J., Flanagan, L. B., Katul, G. G., et al. (2006). A multi-site analysis of random error in tower-based measurements of carbon and energy fluxes. *Agricultural and Forest Meteorology*, 136(1–2), 1–18. <https://doi.org/10.1016/j.agrformet.2006.01.007>
- Running, S., Mu, Q., & Zhao, M. (2017). MOD16A2 MODIS/Terra net evapotranspiration 8-day L4 global 500m SIN grid V006 [Data set]. NASA EOSDIS Land Processes DAAC. <https://doi.org/10.5067/MODIS/MOD16A2.006>
- Sahoo, A. K., Pan, M., Troy, T. J., Vinukollu, R. K., Sheffield, J., & Wood, E. F. (2011). Reconciling the global terrestrial water budget using satellite remote sensing. *Remote Sensing of Environment*, 115(8), 1850–1865. <https://doi.org/10.1016/j.rse.2011.03.009>
- Schimel, D., & Schneider, F. D. (2019). *Flux towers in the sky: Global ecology from space*. John Wiley & Sons, Ltd. <https://doi.org/10.1111/nph.15934>
- Senay, G., Budde, M., Verdin, J., & Melesse, A. (2007). A coupled remote sensing and simplified surface energy balance approach to estimate actual evapotranspiration from irrigated fields. *Sensors*, 7(6), 979–1000. <https://doi.org/10.3390/s7060979>
- Senay, G. B. (2018). Satellite psychrometric formulation of the operational Simplified Surface Energy Balance (Ssebop) model for quantifying and mapping evapotranspiration. *Applied Engineering in Agriculture*, 34(3), 555–566. <https://doi.org/10.13031/aea.12614>
- Senay, G. B., Budde, M. E., & Verdin, J. P. (2011). Enhancing the Simplified Surface Energy Balance (SSEB) approach for estimating landscape ET: Validation with the METRIC model. *Agricultural Water Management*, 98(4), 606–618. <https://doi.org/10.1016/j.agwat.2010.10.014>
- Shiff, S., Helman, D., & Lensky, I. M. (2021). Worldwide continuous gap-filled MODIS land surface temperature dataset. *Scientific Data*, 8(1), 1–10. <https://doi.org/10.1038/s41597-021-00861-7>
- Su, Z. (2002). The Surface Energy Balance System (SEBS) for estimation of turbulent heat fluxes. *Hydrology and Earth System Sciences*, 6(1), 85–99. <https://doi.org/10.5194/hess-6-85-2002>
- Tramontana, G., Jung, M., Schwalm, C. R., Ichii, K., Camps-Valls, G., Ráduly, B., et al. (2016). Predicting carbon dioxide and energy fluxes across global FLUXNET sites with regression algorithms. *Biogeosciences*, 13(14), 4291–4313. <https://doi.org/10.5194/bg-13-4291-2016>
- USDA National Agricultural Statistics Service Cropland Data Layer. (2020). *Published crop-specific data layer [Online]*. USDA-NASS. Retrieved from <https://nassgeodata.gmu.edu/CropScape/>
- Vinukollu, R. K., Wood, E. F., Ferguson, C. R., & Fisher, J. B. (2011). Global estimates of evapotranspiration for climate studies using multi-sensor remote sensing data: Evaluation of three process-based approaches. <https://doi.org/10.1016/j.rse.2010.11.006>
- Wang, K., & Dickinson, R. E. (2012). A review of global terrestrial evapotranspiration: Observation, modeling, climatology, and climatic variability. *Reviews of Geophysics*, 50(2). <https://doi.org/10.1029/2011RG000373>
- Xiao, J., Fisher, J. B., Hashimoto, H., Ichii, K., & Parazoo, N. C. (2021). Emerging satellite observations for diurnal cycling of ecosystem processes. *Nature Plants*, 7(7), 1–11. <https://doi.org/10.1038/s41477-021-00952-8>
- Yang, F., White, M. A., Michaelis, A. R., Ichii, K., Hashimoto, H., Votava, P., et al. (2006). Prediction of continental-scale evapotranspiration by combining MODIS and AmeriFlux data through support vector machine. *IEEE Transactions on Geoscience and Remote Sensing*, 44(11), 3452–3461. <https://doi.org/10.1109/TGRS.2006.876297>
- Yu, Y., Tarpley, D., Privette, J. L., Goldberg, M. D., Rama Varma Raja, M. K., Vinnikov, K. Y., & Xu, H. (2009). Developing algorithm for operational GOES-R land surface temperature product. *IEEE Transactions on Geoscience and Remote Sensing*, 47(3), 936–951. <https://doi.org/10.1109/TGRS.2008.2006180>
- Yuan, W., Liu, S., Yu, G., Bonnefond, J.-M., Chen, J., Davis, K., et al. (2010). Global estimates of evapotranspiration and gross primary production based on MODIS and global meteorology data. *Remote Sensing of Environment*, 114(7), 1416–1431. <https://doi.org/10.1016/j.rse.2010.01.022>
- Zhang, Q., Manzoni, S., Katul, G., Porporato, A., & Yang, D. (2014). The hysteretic evapotranspiration - Vapor pressure deficit relation. *Journal of Geophysical Research: Biogeosciences*, 119(2), 125–140. <https://doi.org/10.1002/2013JG002484>
- Zheng, H., Wang, Q., Zhu, X., Li, Y., & Yu, G. (2014). Hysteresis responses of evapotranspiration to meteorological factors at a diel timescale: Patterns and causes. *PLoS ONE*, 9(6), e98857. <https://doi.org/10.1371/journal.pone.0098857>